JOURNAL OF GEOPHYSICAL RESEARCH, VOL. 92, NO. A13, PAGES 15,093–15,109, DECEMBER 30, 1987

The Upper Atmosphere of Uranus: EUV Occultations Observed by Voyager 2

FLOYD HERBERT, B. R. SANDEL, R. V. YELLE, J. B. HOLBERG, A. L. BROADFOOT, AND D. E. SHEMANSKY

Lunar and Planetary Laboratory West, University of Arizona, Tucson

S. K. ATREYA

Department of Atmospheric and Oceanic Science, University of Michigan, Ann Arbor

P. N. ROMANI

NASA Goddard Space Flight Center, Greenbelt, Maryland

Occultation observations of the upper atmosphere of Uranus by the Voyager 2 ultraviolet spectrometer are analyzed. The measurements extend from 0.5 mbar to about 10^{-6} μbar using the EUV wavelengths $520 \leq \lambda \leq 1700$ Å. H_2 dominates the atmosphere (the approximately 15% He content deduced by the Voyager 2 infrared spectrometer cannot be seen in occultation at these wavelengths) up to the vicinity of the exobase near 1.25 R_U, where atomic H becomes the major constituent. Apparently because of weak eddy mixing, the hydrocarbon mixing ratios are quite small in the measured pressure range, so that the atmosphere is more transparent than those of Jupiter and Saturn. Thus H_2 Rayleigh scattering is the dominant source of opacity in the lower portion of the observed pressure range. The mixing ratio of C_2H_2 is on the order of 10^{-8} there, while only an upper limit ($\leq 10^{-7}$) is available for CH_4. Also, some evidence exists for the possible presence of C_2H_6 at a mixing ratio of several $\times 10^{-8}$. The value of the eddy diffusion coefficient at the homopause is much lower than at Jupiter and Saturn; the best fitting of several photochemical models which were matched to the observations assumed a value of 10^4 cm^2 s^{-1}. This may represent an upper limit. In addition, the two high-latitude occultations indicate little difference in upper atmospheric structure between the day and night hemispheres, despite the constancy of the illumination geometry over recent decades. The atmospheric temperature above about 0.01 to 0.001 μbar is 800 ± 100 K. Because of this high temperature the thermal component of the H exosphere extends to great altitude, with number densities of several hundred cm^{-3} at 2 R_U. This high gas density has important implications for ring dynamics, possibly being responsible for the extreme narrowness and isolation of the visible Uranian rings. The extent and density of the H exosphere and the nonthermal corona (which has an even larger scale height) will also strongly affect the origin and maintenance of the unusual plasma populations observed at Uranus by the Voyager 2 plasma science and low-energy charged particle experiments.

1. INTRODUCTION

1.1. *History*

Previous stellar occultations, observed from Earth at visual wavelengths, have constrained the location and temperature of the 1 μbar level of the Uranian thermosphere near equatorial latitudes [*Elliot et al.*, 1981; *French et al.*, 1983]. The radius found for this pressure level was 26145 ± 35 km in close agreement with the measurements to be reported here.

For extreme ultraviolet (EUV) occultations such as those discussed here, the transmission of the atmosphere is determined by absorption and scattering by H_2 and by absorption by H and hydrocarbons. Earlier observations have indicated low hydrocarbon abundances in the upper atmosphere of Uranus. Infrared and millimeter radio observations have suggested a lower CH_4 abundance in the upper atmosphere of Uranus than at Jupiter and Saturn so that Rayleigh scattering by H_2 is relatively more important [*Teifel*, 1983; *Tokunaga et al.*, 1983; *Orton et al.*, 1983, 1986].

UV spectra taken of Uranus by Earth-orbiting telescopes have been analyzed by a number of groups. *Savage et al.* [1980] determined that the opacities of the upper atmosphere due to aerosols and to H_2 Rayleigh scattering along a vertical path were comparable, while *Caldwell et al.* [1981] concluded that the H_2 opacity was dominant. *Encrenaz et al.* [1986] determined a distinctly subsaturation C_2H_2 mixing ratio at high altitudes in the atmosphere of Uranus. These results suggest that the Uranian atmosphere is clearer at UV wavelengths than those of Jupiter and Saturn, as we also argue below.

Raman scattered H Ly α (which should be present under the same conditions of clarity as Rayleigh scattering) was not visible in International Ultraviolet Explorer (IUE) spectra [*Clarke et al.*, 1986]. This feature has been detected in Voyager 2 ultraviolet spectrometer (UVS) spectra [*Yelle et al.*, 1987] and is further evidence of atmospheric clarity.

1.2. *Occultation Experiment*

The Voyager 2 UVS is an objective grating spectrometer covering the wavelength range 530–1700 Å [*Broadfoot et al.*, 1977]. This range is subdivided into 126 spectral channels of width 9.26 Å, within each of which EUV photons are counted simultaneously. During occultation measurements, each channel is read out every 0.32 s in order to achieve maximal spatial resolution.

At Uranus the Voyager 2 UVS observed one solar and three stellar occultations which probed the planet's upper atmosphere. The initial results from these observations are described in the work by *Broadfoot et al.* [1986]. In this paper we expand the analysis of the solar occultation and the en-

Paper number 7A9033.
0148-0227/87/007A-9033$05.00

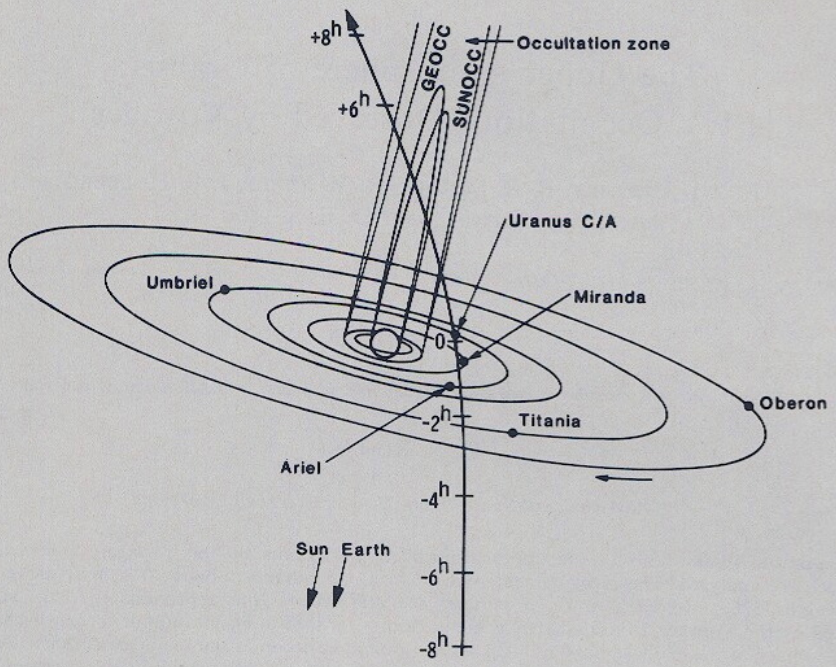

Fig. 1*a*. Occultation geometry; projection into the Voyager 2 orbit plane of the Uranian ring and satellite system with Voyager orbit superimposed. Figure from *Stone and Miner* [1986].

trance and exit occultations of the bright star γ Pegasi (γ Peg). The geometry of these occultations is shown in Figure 1. A third grazing occultation, that of the star ν Geminorum, has not been fully reduced and is not considered here. The solar entrance occultation path intersected the limb at latitude $-3.6°$. (The rather illogical IAU pole-naming convention is used here, and thus it was the south pole that was sunlit at the time of the flyby. This is opposite to the definition used in our earlier paper [*Broadfoot et al.*, 1986]). The exit from occultation was not observed by the Voyager scan platform instruments because of other mission constraints. The γ Pegasi entrance and exit occultations occurred at planetocentric latitudes $-63.7°$ and $+69.7°$, respectively.

The UVS has two apertures: a primary or "airglow" port used for observing planetary atmospheres and an "occultation" port offset 20° from the airglow port and used for viewing the sun. The more sensitive airglow port has a $0.1° \times 0.87°$ field of view (FOV), while the occultation port has a wider $0.25° \times 0.87°$ FOV. The wider occultation port is less sensitive to modulation of the occultation signal due to spacecraft attitude control motion. The stellar occultations were viewed through the airglow port in a photon counting mode. The resulting occultation signal was limited primarily by counting statistics at the 0.32-s time resolution. The solar occultation was observed through the occultation port in an analog charge integrating mode. The solar occultation experiment measured atmospheric transmission over the entire 530–1700 Å range of the detector. The stellar occultations, on the other hand, observed flux only longward of the Lyman limit at 912 Å, due to the absorption of stellar flux in the Lyman continuum by interstellar H.

1.3. *Sources of Opacity*

As the line of sight sinks deeper into the atmosphere, it encounters a varying column abundance (the integral of number density over the line of sight) of one or more atomic and molecular species. As the column abundance increases, the spectrometer records the dimming of the light from the source due to absorption and scattering of light along the path. Thus the observations we describe here differ in a fundamental way from Earth-based stellar occultations, which measure differential refraction by the atmosphere. This is due both to the relatively large EUV cross sections of the species and to the relative closeness of the spacecraft to the planet. For example, at the wavelength of greatest refraction in the UVS range the maximum ray deviation in the accessible height range is about 8 km, as compared to a scale height of about 50 km. In cases where the opacity due to a particular species is due to continuum absorption, the optical depth along the line of sight is given by the product of its column abundance and its absorption cross-section at the wavelength of observation. Even where the absorption is due to unresolved discrete lines (as is the case for Lyman and Werner band absorption in H_2), the transmission is principally a function of column abundance.

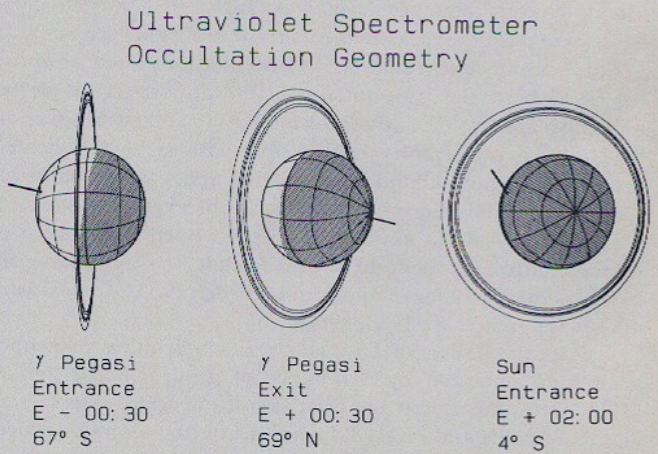

Fig. 1*b*. Occultation geometry; line-of-sight tracks of the three occultations discussed in this paper, projected onto the plane of the sky in the vicinity of Uranus as seen from Voyager 2.

In an isothermal atmosphere with scale height H on a spherical planet at radius $r \gg H$, the column abundance along the line of sight is given by $n_0\ (2\pi Hr)^{1/2}$ [e.g., *Chamberlain*, 1963], where n_0 is the local number density of absorber at the lowest point on the line of sight. In a real atmosphere some adjustment is necessary for altitude variation of temperature and gravity, and the analysis must also self-consistently estimate H. Since the occultation observation consists of a series of absorption measurements over a sequence of parallel ray paths, the variation of n_0 as a function of height in the atmosphere can be deduced if the relevant absorption cross sections are known. Opacities of interest in this investigation are plotted in Figure 2 and are discussed below.

Because the absorption cross section of H_2 is a strong function of wavelength, a large range of column abundance can be investigated by the occultation technique. For $530 \leq \lambda \leq 800$ Å, the absorption cross section σ is approximately 5×10^{-18} to 10^{-17} cm^2. Absorption by the Lyman and Werner band system varies between near transparency and nearly complete opacity over the wavelength range $700 \leq \lambda \leq 1100$ Å for column densities in the range 10^{13} to 10^{21} cm^{-2}, depending on temperature. For $1200 \leq \lambda \leq 1700$ Å, however, Rayleigh scattering is the only source of opacity, at least for temperatures less than a few hundred degrees, with $2 \times 10^{-25} \leq \sigma \leq 3 \times 10^{-24}$ cm^2. This means that column abundances in the range of 10^{16} to 10^{25} cm^{-2} can in principle be determined by these occultation measurements, if the range $0.1 \leq \tau \leq 2$ is measurable. As will be seen in later sections, the scale length for converting column densities to number densities is about 10^9 cm in the upper part of the range probed here and is about 3×10^8 cm in the lower portion. Thus the accessible number density range is $10^7 \leq n_{H_2} \leq 3 \times 10^{16}$ cm^{-3} at Uranus. Using the results of later sections, these are pressure levels of 10^{-6} to 500 μbar.

The continuum absorption cross section for atomic hydrogen varies from 1.5 to 6×10^{-18} cm^2 over the range $530 \leq \lambda \leq 912$ Å. Thus number densities around $n_H \simeq 2$ to 7×10^8 cm^{-3} (for scale heights around 500 km) can be determined, if the H_2 continuum and Lyman-Werner band absorption in this wavelength region can simultaneously be found.

Other species one might expect to detect in the upper atmosphere of a gas giant planet such as Uranus are low molecular weight constituents such as CH_4, its photochemical byproducts such as C_2H_2, C_2H_4, and C_2H_6, and possibly also N, N_2, or NH_3 and its byproducts. However, the low tropospheric temperatures at Uranus' heliocentric distance and possibly other effects seem to limit the abundance of these constituents in the upper atmosphere, as will be discussed in greater detail in later sections. Typical absorption cross sections of 10^{-19} to 10^{-16} cm^{-2} for the hydrocarbons lead to a detectable number density range of several times 10^6 to 10^{10} cm^{-3}.

Helium is also known to be present [*Hanel et al.*, 1986; *Broadfoot et al.*, 1986] but its absorption spectrum is invisible to the UVS because of the absence of a continuum absorption in the 530- to 1700-Å range.

1.4. *Analysis Techniques*

Because of the overlap in wavelength of the absorptions of the species expected to be present, column abundance as a function of height cannot be directly determined for any individual constituent, although H_2 comes close to this separability. Moreover, the atmospheric scale height must be self-consistently estimated along with number densities from the column abundances, and the assumption of a constant temperature made in the discussion of the previous section is only an approximation. Consequently, the inversion of the observed light curves to atmospheric density profiles is neither direct nor unique.

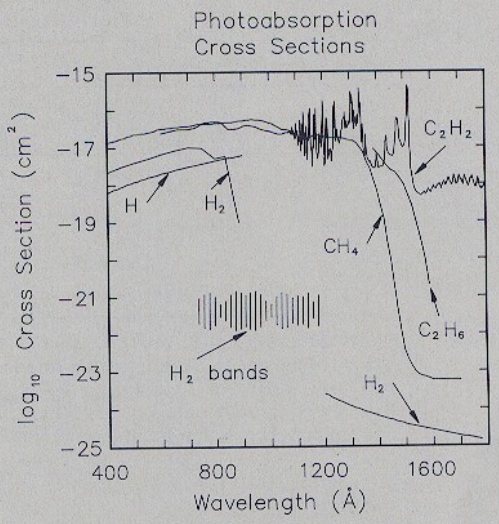

Fig. 2. Photoabsorption cross sections as a function of wavelength for the absorbing species relevant to the Uranian upper atmosphere. Hatched region labeled H_2 bands is merely symbolic rather than denoting a particular cross-section value. H_2 band absorption actually consists of a great many unresolved lines of highly variable cross section whose average behavior very approximately mimics a continuous absorption with cross section intermediate between the H_2 continuum and H_2 Rayleigh scattering.

The procedure we have elected to use for the analysis of the occultation light curves was to generate number density versus height profiles for a group of assumed constituents and then to model the occultation geometry and absorption process to obtain corresponding model light curves at each UVS wavelength. This procedure was repeated for different atmospheric profiles in order to match the model light curves to the observed ones. The sensitivity of the model fit to differences in atmospheric models is also tested by this procedure. This approach is the same as that used at Saturn [*Smith et al.*, 1983] and Titan [*Smith et al.*, 1982] and is similar to that used by *Atreya et al.* [1979] and *Festou et al.* [1981] at Jupiter.

In order to maximize our models' flexibility, we initially generated the atmospheric profiles as simple parametric functions. Once an approximate profile was found for each species more accurate profiles were parameterized by specifying the temperature at several pressure levels and a value for the number density of each species at some height. With $T(p)$ interpolated between these points by a function of the form $T = T_0(p/p_0)^\alpha$, number densities n_i were found by piecewise analytically integrating the hydrostatic equation (including centrifugal acceleration and the variation of gravity with altitude)

$$\frac{n_i}{n_{0i}} = \left\{1 + \frac{\alpha m}{kT_0}\left[GM\left(\frac{1}{r} - \frac{1}{r_0}\right) + \frac{\Omega^2}{2}(r^2 - r_0^2)\right]\right\}^{(1-\alpha)/\alpha} \quad (1)$$

The hydrostatic equation is valid over the altitude range considered here. Here m is the assumed mean molecular weight (below z = 500 km, assuming 15 mol % He; otherwise, it is the molecular weight of species i); the subscript zero denotes values at the bottom of the altitude interval and the other symbols are assigned conventionally. The value of GM is from *Tyler et al.* [1986], and the rotation period of 17.24 hours is from *Warwick et al.* [1986]. For polar occultations (such as those of γ Peg) the Ω^2 factor would normally be multiplied by

TABLE 1. Values of $T(p)$ From Which the Models in Figure 7*b* Were Derived

γ Peg Measurements			Best Compromise			Solar Occultation		
P, μbar	T, K	α	P, μbar	T, K	α	P, μbar	T, K	α
10^4	63		10^4	63		10^4	63	
51	120	−0.122	51	120	−0.122	51	120	−0.122
1	200	−0.130	3.3	170	−0.127	10	150	−0.137
0.2	500	−0.569	0.5	500	−0.572	1	475	−0.501
2×10^{-4}	750	−0.059	10^{-5}	800	−0.043	10^{-5}	800	−0.045
$n_H(1720\text{ km}) = 3.3 \times 10^8\text{ cm}^{-3}$			$n_H(1720\text{ km}) = 3.3 \times 10^8\text{ cm}^{-3}$			$n_H(3200\text{ km}) = 4.1 \times 10^7\text{ cm}^{-3}$		

At 320 km, $p_{H_2} = 51$ μbar; $n_{CH_4} = 5 \times 10^8$ cm^{-3} (upper limit); $n_{C_2H_2} = 2.4 \times 10^7$ cm^{-3}; and $n_{C_2H_6} = 1.5 \times 10^8$ cm^{-3}. At 200 km (model standard reference point), $p_{H_2} = 0.81$ mbar; $n_{CH_4} = 1.2 \times 10^{10}$ cm^{-3}; $n_{C_2H_2} = 5 \times 10^8$ cm^{-3}; and $n_{C_2H_6} = 3 \times 10^9$ cm^{-3} (uniformly mixed model). All altitudes are measured from an equatorial radius of 25,550 km. The atmosphere is assumed to be diffusively separated above $z = 500$ km; below that point it is assumed to be well mixed with a mean molecular mass of 2.3 amu.

$\cos^2 \beta$, with β the latitude, but here we will adjust the polar occultation altitude scales instead. The value of α is adjusted to interpolate correctly between the bottom and the top of each pressure interval. The altitude integral evaluated inside the brackets is broken up into separate intervals if the homopause falls into the range of integration. With the temperature determined as described in sections 2.2 and 2.4 at the top and bottom of the thermosphere (and a third point at 63 K and 10 mbar [*Hanel et al.*, 1986; *Tyler et al.*, 1986]), specification of a few $T(p)$ values at intermediate pressures suffices to determine the proper height scale between the high and low altitude measurements and also to match estimates of the H_2 column abundance. Values for models which have fit the data reasonably well are given in Table 1.

Altitudes quoted throughout this paper will be expressed as heights above a zero level at the planetocentric distance of 25,550 km, by convention defined as 1 R_U. For latitudes different from zero, the altitude is given as the equatorial height of the centrifugal-acceleration-adjusted equipotential passing through the point in question. The method of calculation of the equipotentials was given by *Broadfoot et al.* [1986], who used a reference radius of 26,200 km in their computations.

2. Solar Occultation

2.1. *Description of the Observation*

The entrance solar occultation observation was carried out from approximately 2011 to 2025 Spacecraft Event Time (SCET) on January 24, 1986 (about 2 hours after closest approach), at a slant range of 1.7×10^5 km to the point of observation at planetocentric latitude −3.6°. Useful data were obtained through the occultation port at line of sight altitudes from about 150 to 6500 km above 1 R_U. The speed of descent of the line of sight through the atmosphere varied from 8.2 to 7.6 km s^{-1}, yielding a nominal height resolution of about 2.5 km with the 0.32-s sampling rate. However, the projection of the solar disk subtended about 82 km in altitude, so that the height resolution is somewhat degraded.

A more serious difficulty faced by the analysis, however, is the near saturation of the detectors by the high solar EUV flux. Careful modeling of the instrumental response to high flux levels [*Sandel and Broadfoot*, 1986] was required in order to estimate the flux values from the observed counting rates, particularly for the H Ly α line. The procedure for deconvolution of the observed spectra to remove the effects of instrumental scattered light depends on the accuracy of the counts-to-flux modeling process. As a result, the derived spectra have reduced accuracy in the vicinity of the H Ly α line, which impacts severely the determination of CH_4 and C_2H_6 abundances from the solar occultation data. For example, the scattered light at 1350 Å, where estimates of CH_4 abundance have been made in the past [*Smith et al.*, 1982, 1983], is 0.7% (per channel) of the integrated H Ly α flux. By comparison the ratio of 1350 Å flux (per channel) to net H Ly α flux in the raw solar spectrum is approximately 1%. In the linear range of the instrument, the appropriate subtraction can be made accurately, but when the ratio of the instrumental gain at the strong H Ly α line to that at other wavelengths is not well determined, the correction process is less accurate.

The conclusions presented in this paper are based on the best analysis of this correction that is presently available. However, some improvement may be possible and studies are under way to increase the accuracy of our analysis. If significant improvements result, they will be reported on at a later date.

Because of the wide dynamic range of the UVS detector and the great variation of opacity with wavelength, the occultation observation probes a large range of atmospheric pressure. In the following sections we analyze these observations in terms of the major opacity sources.

2.2. *H_2 Continuum*

As was mentioned in section 1.3, the continuum absorption cross section of H_2 varies from 5×10^{-18} cm^{-2} at 530 Å to 10^{-17} cm^2 at 700 Å. Consequently, in principle, H_2 should become detectable by occultation at a column abundance of some fraction (depending on the signal-to-noise ratio) of 10^{17} cm^{-2}. In fact, H_2 absorption first becomes noticeable at an altitude of about 6500 km, where the inferred column density is about 6×10^{15} cm^{-2} and the deduced number density is about 6×10^6 cm^{-3}. The H_2 continuum region of the spectrum becomes nearly opaque at an altitude of about 4000 km, where the column and number densities are about 5×10^{17} and 5×10^8, respectively. The most reliable determination extends over the altitude range of 4500 ($n_{H_2} = 1.8 \times 10^8$) to 5500 km ($n_{H_2} = 3 \times 10^7$), however.

The fit to the data of the profile from which these numbers are taken is shown in Figure 3. The adopted profile has a temperature of 800 K at this altitude and was used to compute a model light curve which is plotted with the observed light curve in two different wavelength ranges. Also shown are model light curves computed from H_2 profiles which agreed with the 800 K profile near 5000 km, but differed in assumed temperatures of 700 and 900 K. Note that the curves cross at altitudes below 5000 km because of differences in effective

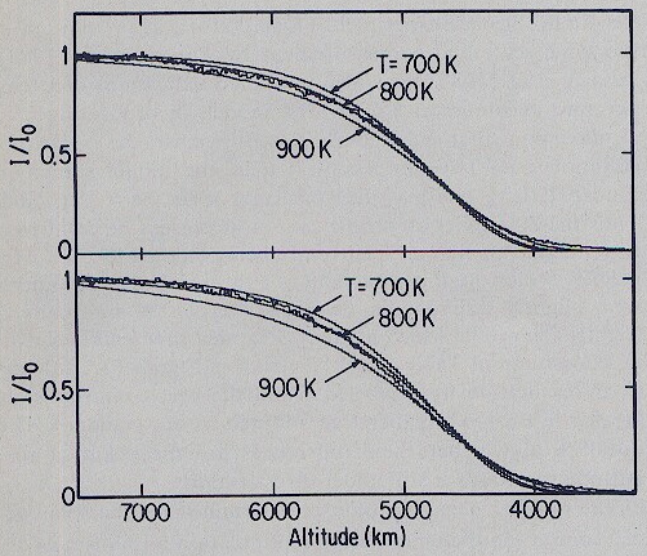

Fig. 3. Exospheric temperature determination. Solar occultation light curves (jagged curves) measured over the ranges $569 \leq \lambda \leq 708$ Å and $717 \leq \lambda \leq 819$ Å, measuring opacity due to continuum absorption by H_2. Superimposed model curves (smooth curves) were computed for exospheric temperatures of 700, 800, and 900 K, normalized to the same number density at an altitude of 5000 km.

path length caused by the differing scale heights. The noticeably inferior fit of the 700 and 900 K profiles suggests that the reliability of the 800 K temperature estimate at this altitude is within ± 100 K. The temperature and H_2 density values derived from this fit are shown in Figure 4.

2.3. *H_2 Lyman and Werner Bands*

The wavelength range 912 to 1100 Å is useful for measuring extinction due to the Lyman and Werner bands of H_2. Absorption in the H_2 band systems has been described by *Festou et al.* [1981] and by *Smith et al.* [1983]. Using these wavelengths n_{H_2} is measurable over the altitude range of about 1000 ($n_{H_2} = 3 \times 10^{12}$) to about 2500 km ($n_{H_2} = 2 \times 10^{10}$). However, at the wavelengths nearer H Ly α at 1216 Å the accuracy of the solar occultation measurements is compromised by the combination of instrumental scattering of H Ly α and the nonlinearity of the detector response. Consequently, only the shorter wavelength portions of the Lyman-Werner bands are plotted in Figure 5*b*. As in the previous section, the observed light curves are overplotted by model light curves produced from our preferred H_2 profile. Because of the instrumental scattering and nonlinearity, however, the fit is not as good as would otherwise be expected. While the appearance of Figure 5*b* suggests that the model temperature is too low for $1000 \leq z \leq 2500$ km, the constraint of n_{H_2} at higher and lower altitudes plus the hydrostatic equation limit the freedom of the fit. The approximate temperature and H_2 density values derived from this fit are shown in Figure 4.

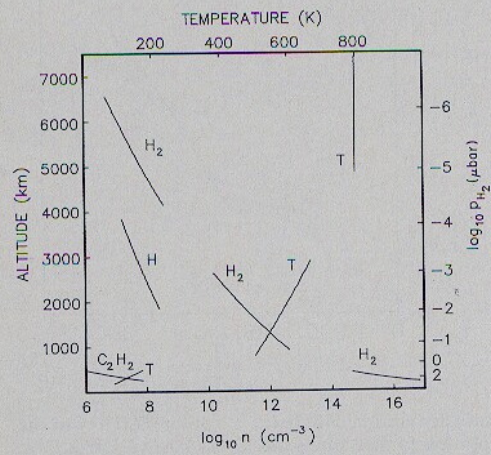

Fig. 4. Number density versus altitude profiles. Densities of H_2, H, and C_2H_2 as well as the atmospheric temperature, all directly inferred from the occultations, are plotted against altitude. Right-hand scale shows H_2 partial pressure (p_{H_2}).

2.4. *H_2 Rayleigh Scattering*

Because of the low abundance of hydrocarbons and other continuum absorbers above the 1 mbar level, the upper atmosphere of Uranus is more transparent than those of gas giant planets visited so far. Consequently Rayleigh scattering, despite its small cross section, becomes a major source of opacity in the altitude range 200 ($n_{H_2} \simeq 7 \times 10^{16}$) to 400 km ($n_{H_2} = 6 \times 10^{14}$). This is a new feature in the UV occultations of the outer planets and allows us to determine the density and temperature of the major constituent, H_2, in the stratosphere.

The characteristic wavelength dependence of Rayleigh scattering can be seen in Figure 6, where an observed I/I_0 spectrum (defined as a spectrum which has been divided by a spectrum of the light source, here the sun) is compared with the Rayleigh scattering cross section scaled by an appropriately picked H_2 column density. Although other sources of opacity are present (notably C_2H_2), the contribution of Rayleigh scattering is clear.

The match between observed and model light curves in the

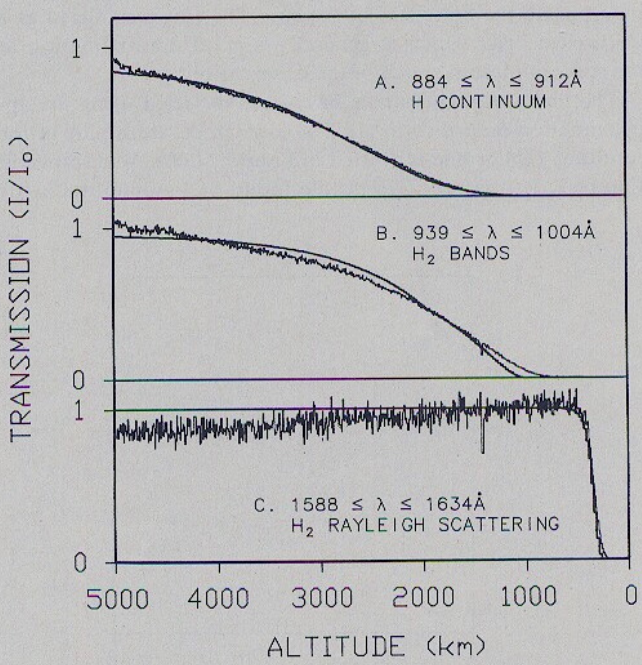

Fig. 5. Solar occultation (thin curves) and superimposed model (thick curves) light curves. Data contains an offset at about 5000 km altitude, which is due to an insufficiently corrected pointing offset which moved the sun's image relative to the spectrograph slit. (*a*) $884 \leq \lambda \leq 912$ Å. Combination of H_2 bands and H continuum absorption. (*b*) $939 \leq \lambda \leq 1004$ Å. H_2 Lyman and Werner band absorption. (*c*) $1588 \leq \lambda \leq 1634$ Å. Rayleigh scattering opacity. Reduced values of I/I_0 above 1500 km in Figure 5*c* are caused by inaccuracies associated with scattered H Ly α light and is not significant.

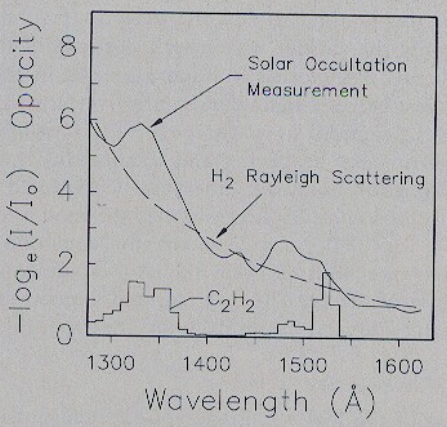

Fig. 6. Least squares fit of model opacity to observed transmission spectrum. Solar occultation is plotted as $-\log_e I/I_0$ as a function of λ observed low in the upper atmosphere. A function of the form $\Sigma c_i\sigma_i$ for $i = H_2$ and C_2H_2 was fit to $-\log_e I/I_0$, and the partial opacities $c_i\sigma_i$ are plotted separately. Match of the C_2H_2 profile is apparent, as is the general Rayleigh scattering shape of the observed I/I_0.

wavelength interval $1588 \leq \lambda \leq 1634$ Å is shown in Figure 5c. The absorption due to hydrocarbons is negligible in this interval, and thus we use it to analyze the altitude profile of H_2. The best fitting scale height is about 50 km, which implies a temperature of about 120 K at this altitude, assuming a 15% He abundance [*Hanel et al.*, 1986] and effective g computed from the measured rotation rate [*Warwick et al.*, 1986] and mass [*Tyler et al.*, 1986]. Although the projection of the solar disk subtends 82 km at the distance of the atmosphere in this observation, altitude resolution significantly better than this is possible because our models of the occultation measurement incorporate the finite size of the sun. The sun is modeled as a featureless disk, which is generally a good approximation at the solar minimum epoch of the observations.

The observed light curves have been modeled using the approximation described in (1). The low-temperature part of the resulting $T(p)$ profile is plotted in Figure 7 (left). Also shown in Figure 7 (left) is the $T(p)$ profile found at lower altitudes by the Radio Science experiment [*Lindal et al.*, 1986] plotted at the same scale and a measurement by *French et al.* [1983]. *Sicardy et al.* [1985] have also published indications of a temperature maximum at 8 μbar. $T(p)$ models incorporating such a maximum that have been tested against the solar occultation data have fit less well than the model shown in Figure 7 (left), but may be consistent with the γ Peg data. Thus the Sicardy et al. profile cannot at present be confirmed or refuted. This matter is currently being studied further. $T(p)$ profiles which fit the solar and γ Peg entrance occultations were slightly different so they are overplotted in Figure 7 (right). The profile which fits the γ Peg measurements is shown in left column in Table 1 and labeled a in Figure 7 (right); the solar occultation fit is labeled c and the best compromise is labeled b. Profile b is therefore adopted as our standard. The question of whether these differences are the result of real latitude variations is still under investigation.

The number density profile as determined for the solar occultation using the temperature interpolation formalism as described above is plotted in Figure 4. This profile correctly spaces the UVS observation points from the Voyager Radio Science measurement of 10 mbar at an equatorial radius of 25,670 km (Radio Science team, private communication 1986), within a few tens of kilometers. The apparent layer structure near 0.3 mbar in the Radio Science $T(p)$ profile (Figure 7 (left)) falls near the upper boundary of the Radio Science observations, where observational constraint is weak. Our profile's 1 μbar point also agrees well with the *Elliot et al.* [1981] point at 26,145 km radius.

2.5. *Atomic H*

Atomic hydrogen is a constituent of vital importance to the understanding of the upper atmosphere of Uranus. As will be discussed in greater detail in later sections, it is expected to significantly affect the orbital evolution of the rings and probably influences the lower magnetosphere.

However, the direct determination of n_H is complicated by the overlap between the continuum absorption of H and the Lyman-Werner band absorption of H_2 in the range 700 to 912 Å. Fortunately, n_{H_2} may be determined as described above and then the additional absorption in the 700- to 912-Å region due

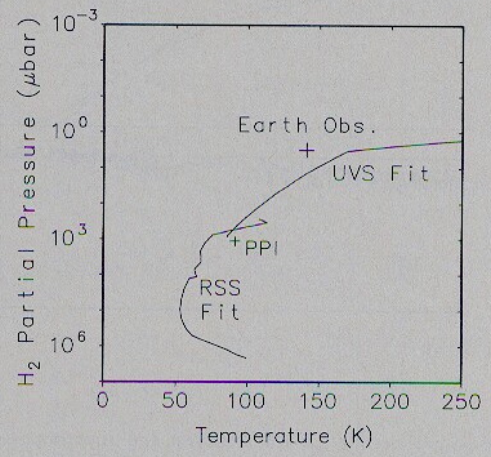

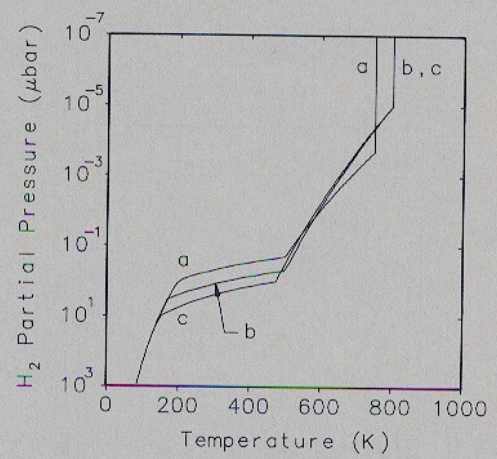

Fig. 7. $T(p)$ profiles deduced for the Uranian atmosphere. (Left) Values deduced here (labeled UVS) for $T(p)$ low in the atmosphere are compared with the results of *Lindal et al.* [1986] (RSS) plotted to the same scale. Cross labeled Earth Obs. indicates the half-light measurement of *French et al.* [1983] and the cross labelled PPI is from *Lane et al.* [1986]. Wiggles in the Lindal et al. plot are thought to be due to local aerosol condensation thermodynamics; the smooth part of the variation is the relevant comparison for the UVS determination. (Right) $T(p)$ plotted over the whole upper atmosphere. Several alternatives are given that fit different data sets. Alphabetic labels correspond to the models summarized in Table 1.

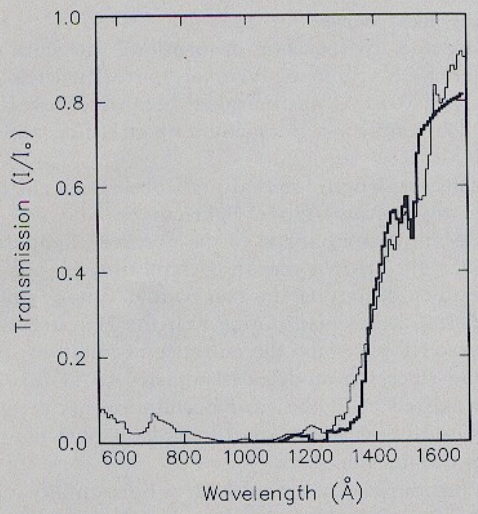

Fig. 8. I/I_0 spectra showing C_2H_2 absorptions. Light line shows the observed spectrum; the dark line the model which was matched to it. Observed spectrum is an average over altitudes between 295 and 375 km. Values for $\lambda < 1000$ Å are spurious.

to H estimated. In this way the H profile over the altitude range 2000 ($n_H = 2 \times 10^8$) to 4000 km ($n_H = 1.4 \times 10^7$) was determined. The profile used to match the observed light curve assumed a temperature the same as that determined from the H_2 analysis. Figure 5*a* demonstrates that a temperature of 800 K is consistent with the H measurements as well as with the H_2 data, though not as sensitively tested. The H profile is shown over the 2000- to 4000-km range in Figure 4.

2.6. *Hydrocarbons*

The most clearly evident spectral signature of a hydrocarbon is that of C_2H_2, near 1500 Å. At UVS resolution this feature, which actually consists of absorptions at 1477 and 1518 Å, is just barely resolved. Although C_2H_2 has strong absorptions at other wavelengths, they are much harder to distinguish from those due to other constituents, so in fitting C_2H_2 we shall concentrate on this one region.

Figure 8 shows a comparison of an averaged I/I_0 spectrum (light curve), made from data taken near the end of the occultation measurement, with a corresponding model spectrum (dark curve). There are a number of deviations between the two curves that probably result from the dataprocessing problems discussed earlier, but it appears that the deepest absorption feature in the data (coincident with the deepest feature in the model, at about 1500 Å) may be real. We cautiously interpret the similarity between the 1500 Å features as a detection of C_2H_2. The C_2H_2 mixing ratio of 10^{-8} was estimated by adjusting the model C_2H_2 abundance to maximize the similarity between the two curves (at this and other occultation altitudes). The other local minimum in the data, near 1450 Å, does not occur at the same wavelength as the C_2H_2 absorption expected at 1477 Å and so we regard it as spurious.

Because C_2H_2 is the result of a network of photochemical reactions the mathematical form of its altitude distribution is not self-evident. In the present section, we assume for simplicity that the atmosphere is well mixed in the hydrocarbon visibility region, so all scale heights are taken equal to that of H_2, i.e., 50 km. The intent is that the number densities we derive thereby describe in some average sense the hydrocarbon distributions over their region of greatest detectability. As an alternative, in section 4.3.2 we take a more accurate but model-dependent approach, in which photochemical model distributions are adjusted to fit the occultation light curves.

The altitude range over which C_2H_2 is visible is approximately 200 ($n_{C_2H_4} \simeq$ several $\times 10^8$) to 400 km ($n_{C_2H_2} \simeq$ several $\times 10^6$). The best fit mixing ratio $n_{C_2H_2}/n_{H_2}$ in this altitude range is approximately 10^{-8}. The corresponding $n_{C_2H_2}$ profile is plotted in Figure 4.

Presumably, the source for this C_2H_2 is CH_4, diffusing up to this altitude from a cold trap at lower levels in the atmosphere. The effects of CH_4 absorption are difficult to discern in the occultation data because the abundance of CH_4 is low and its absorption spectrum is relatively featureless. Its continuum absorption drops rapidly longward of 1350 Å, but the analysis of the "knee" that this induces in I/I_0 spectra such as Figure 8 is hindered by the inaccuracies in removing scattered H Ly α described earlier. Comparison of model and observed I/I_0 spectra in the 1090 to 1170 Å and 1250 to 1350 Å regions and over the 300- to 500-km altitude range indicates an upper limit for the average n_{CH_4}/n_{H_2} mixing ratio in the vicinity of 10^{-7}. The shorter wavelength range is best fit by this mixing ratio, but the longer wavelengths are best fit by considerably less CH_4. Consequently, we interpret our results as establishing an upper limit of 10^{-7} for n_{CH_4}/n_{H_2}. As with C_2H_2, the model profiles assume a CH_4 scale height that is the same as that of H_2, namely, 50 km.

The other hydrocarbon constituent for which there seems to be some evidence is C_2H_6. The absorption cross section of C_2H_6, like that of CH_4 drops longward of 1350 Å, but the falloff of the C_2H_6 cross section is not nearly so rapid with increasing wavelength as that of CH_4. Consequently, C_2H_6 can in principle be distinquished from CH_4. The most noticeable result of the presence of C_2H_6 is a decrease in the slopes of the 1350 to 1450 Å regions of model I/I_0 spectra, bringing them into closer agreement with the observed spectra. The greatest degree of similarity seems to be attained at a $n_{C_2H_6}/n_{H_2}$ about half the value of the n_{CH_4}/n_{H_2} upper limit, i.e., somewhere near several $\times 10^{-8}$. The variation produced in model I/I_0 spectra by including $n_{C_2H_6} = 2 \times 10^{-8}\, n_{H_2}$ is illustrated in Figure 9. This is only a rough approximation, however, because the CH_4 and C_2H_6 absorption profiles resemble each other, and thus the relative amounts of absorption caused by the two species cannot be uniquely well determined. Because

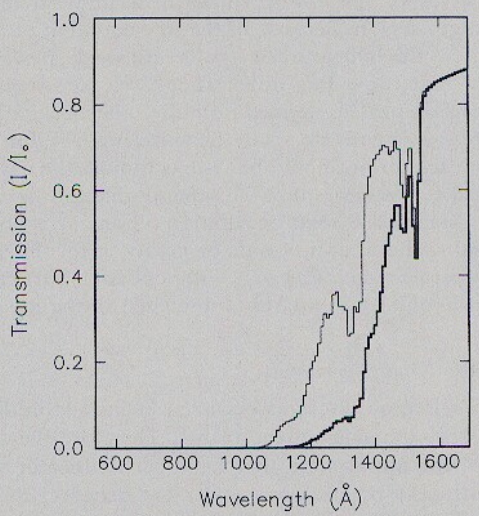

Fig. 9. Comparison of model spectra showing influence of C_2H_6 on the shape of I/I_0. Both curves are synthetic spectra including C_2H_2 absorption and H_2 Rayleigh scattering and corresponding approximately to the model shown in Figure 8. Dark curve shows a model which also includes C_2H_6 with a mixing ratio of 2×10^{-8} relative to H_2.

the CH_4 and C_2H_6 profiles are so uncertain, we have omitted them from Figure 4.

3. Stellar Occultations

The entrance occultation of γ Pegasi lasted from approximately 1721 to 1728 SCET on January 24, 1986, at planetocentric latitude $-63.7°$, with the exit occurring from 1815 to 1822 at latitude $+69.7°$. The vertical speed of the line of sight was 17.8 km/s for both entrance and exit, giving a nominal height resolution of 5.7 km, although photon counting statistics did not allow taking full advantage of this resolution. The slant ranges to the planetary limb were approximately 10^5 km and for these occultations the airglow port was used.

The γ Peg occultation data have one significant advantage over the solar occultation data: linearity. Because the γ Peg flux level was within the linear response range of the UVS, it was possible to remove accurately the effects of light scattering in the instrument. However, the lower light level coupled with the higher line-of-sight velocity yielded a significantly lower signal-to-noise ratio due to counting statistics. Moreover, the opacity of interstellar and interplanetary neutral H resulted in the absence of signal for $\lambda \leq 912$ Å, while the low detector sensitivity longward of 1200 Å yielded low counting rates in that region. Finally, for the γ Pegasi exit, magnetospheric charged particle bombardment raised the dark count rate.

3.1. *H_2 Bands*

Although the $\lambda \leq 912$ Å cut-off of the γ Peg data precludes measurement of either H or H_2 continuum absorption, the Lyman and Werner bands of H_2 allow determination of the altitude profile of H_2 at the latitudes of $-63.7°$ and $69.7°$ where the entrance and exit occultations of γ Peg occurred. Light curves for this wavelength region are shown in Figure 10. The model light curves were generated with number density profiles derived from the γ Peg model of Table 1, except for approximate correction to the equivalent gravitational equipotentials appropriate at the latitudes of observation as described previously.

3.2. *Long Wavelengths: H_2 Rayleigh Scattering and Hydrocarbons*

Figure 10*c* shows a comparison of observed and modeled light curves of the γ Peg entrance occultation in the long wavelength region. Because of the low counting rate, the constraints on the hydrocarbon profile are weak. Nevertheless, it appears that the γ Peg observations are consistent with the hydrocarbon profiles derived from the solar occultation.

There is also consistency in the wavelength region where H_2 Rayleigh scattering should be visible, though the data are very noisy there. It appears that the same profile zero level used for the near-equatorial solar occultation (upon correction for geopotential shape) is appropriate or nearly so for the two higher latitude measurements as well, with a possible vertical offset of at most about 30–50 km, as is discussed in the following section.

3.3. *Day-Night Symmetry*

Both γ Peg occultations occurred at high latitudes, but on nearly opposite sides of the planet. Therefore they probe regions of the atmosphere that have been either in sunlight (γ Peg entrance) or darkness (exit) for decades. Surprisingly, there is little difference between the two observations. Figure 11*a* shows light curves observed during the entrance occultation, and Figure 11*b* shows the same information obtained at exit. The top panel of each figure shows the I/I_0 light curve for $958 \leq \lambda \leq 1004$ Å (H_2 bands) and the bottom panels show the light curves for $1254 \leq \lambda \leq 1356$ Å (H_2 Rayleigh scattering and hydrocarbon absorption). The data quality in the wavelength region of relatively pure Rayleigh scattering ($1588 \leq \lambda \leq 1650$ Å) was marginal because of low light intensity, which resulted in poor counting statistics, and so is not shown.

In each wavelength interval both observed light curves are matched by the same model light curves. This was done primarily to allow comparison of the observed light curves with each other; for obvious reasons overplotting the two observed light profiles onto one another would not be informative. Nevertheless, it is worth noting that the H_2 band light curve fits the model better for the entrance occultation; this is not surprising since the model was adjusted to fit this case. The model adjusted to fit the solar occultation fits the γ Peg exit occultation about as well as the model shown fits the γ Peg entrance occultation.

After positioning each model curve horizontally for the best fit at the Rayleigh scattering wavelengths, the absolute altitude coresponding to a standard reference point of the model (corresponding to approximately 0.9 mbar) was found. The absolute radii for the model reference points were $25{,}750 \pm 10$ km (solar), $25{,}290 \pm 20$ (γ Peg entrance), and $25{,}240 \pm 40$ (γ Peg exit). In order to compare these values, a very approximate model (± 40 km) for the equipotentials as modified by centrifugal and Coriolis acceleration [*Broadfoot et al.*, 1986] was used. At each point, the equatorial altitude of the equipotential passing through the observed absolute altitude at the appropriate latitude was determined. The calculation of equipotentials (which include centrifugal acceleration) used a rotation period of 17.3 hours and the gravitational constants given by *Broadfoot et al.* [1986]. This equatorial altitude is referred to here as the "equivalent equatorial altitude" of the observed ray height. The equivalent equatorial radii of the model reference points as matched to the occultation light curves are 25,675 km for the γ Peg exit observation and 25,725 km for the γ Peg entrance occultation. These numbers can be compared to the level of the solar occultation at 25,750 km. These estimates may be regarded as showing that isobars nearly coincide (within the errors of observation) with equipotentials. However, they are only marginally consistent, a fact which will be investigated in future work for the possibility of constraining the gravitational moments and/or atmospheric mass motion. Also the gravitational constants assumed [*Broadfoot et al.*, 1986] need further refinement.

In any case, the high degree of symmetry of the ambient H_2 atmosphere among the light and dark side and terminator occultations implies that scale heights (adjusted for the latitude dependence of gravity) and hence temperature profiles are similar over the range of altitudes from 200 to 3000 km. This result is surprising given the preponderance of heating mechanisms that are confined to the illuminated side of the planet. The observed similarity between light and dark sides indicates that horizontal energy transport dominates over radiative losses, or that heat sources other than direct solar radiation are important. Since the electroglow is absent on the dark side, it cannot provide the dominant heat source there, unless there is efficient horizontal heat transport. Both γ Pegasi occultations occurred well away from the auroral zones. Therefore direct auroral heating of the atmosphere cannot be responsible for the observed symmetry. The similarity between the thermal structures in the two hemispheres was also noted by *French et al* [1983], who suggested that it implied efficient global circulation. Models of global heat flow in the thermosphere are needed to address this question. In section 4.1 we discuss thermospheric heating in more detail.

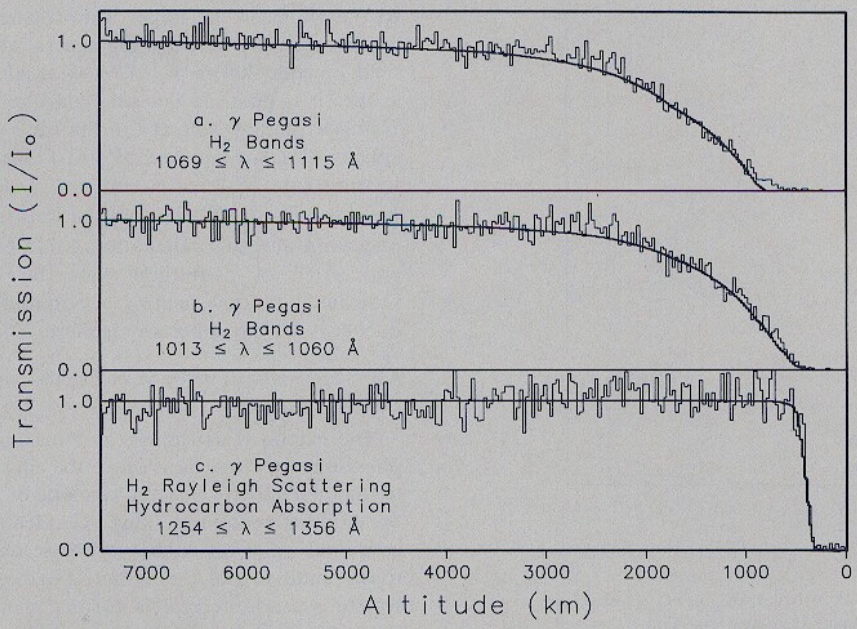

Fig. 10. γ Peg occultation and superimposed model light curves. (*a*) $1069 \leq \lambda \leq 1115$ Å. H_2 Lyman and Werner band absorption. (*b*) $1013 \leq \lambda \leq 1060$ Å. H_2 Lyman and Werner band absorption. (*c*) $1254 \leq \lambda \leq 1356$ Å. Rayleigh scattering and hydrocarbon absorption opacity. Altitude scale has been converted to equivalent equatorial values.

4. Discussion

4.1. *Exospheric Temperature*

As at Uranus, the exospheric temperatures at Jupiter and Saturn are also high [*Festou et al.*, 1981; *Festou and Atreya*, 1982; *Smith et al.*, 1983]. The high temperatures require some explanation since the energy deposited in the upper atmosphere by solar EUV radiation is several orders of magnitude too small to produce the necessary heating [*Strobel and Smith*, 1973]. We can estimate the energy flux Q required to produce the observed temperatures from the equation

$$T_\infty^{(s+1)} = T_0^{(s+1)} + (s+1)Q\Delta z/A \qquad (2)$$

where T_∞ is the exospheric temperature, T_0 is the temperature at z_0, the base of the thermosphere, and A and s are parameters related to the thermal conductivity of H_2 and have values of $A = 252$ erg cm^{-1} s^{-1} K$^{-(s+1)}$ and $s = 0.751$ [*Hanley et al.*, 1970]. Equation (1) is derived under the assumption that the energy flux is deposited in a thin layer a distance Δz above z_0 and conducted downward to z_0 where it is radiated away [*Hunten and Dessler*, 1977]. Using values of 800 and 100 K for T_∞ and T_0 for Uranus and estimating $\Delta z \simeq 2000$ km from the occultation results we infer a column heating rate of 0.08 ergs cm^{-2} s^{-1} [*Yelle et al.*, this issue], compared to 0.004 ergs cm^{-2} s^{-1} for direct heating by ionizing EUV [*Broadfoot et al.*, 1986].

A common assumption is that the heating of the upper atmospheres of the outer planets is related to the electroglow phenomenon [*Smith et al.*, 1983; *Shemansky and Smith*, 1986; *Broadfoot et al.*, 1986]. In this scenario, dissociation of H_2 by low-energy electrons associated with the electroglow produces both upward and downward fluxes of heat and atomic hydrogen. The upward flux has been postulated to be the source of the nonthermal corona (see section 4.5) while the downward flux would presumably account for the presence of the H distribution observed by the occultation experiment [*Broadfoot et al.*, 1986].

Figure 12 shows several models of the thermospheric atomic hydrogen density profile. These profiles are solutions of the one-dimensional continuity and momentum equations. The free parameters in the calculations are the downward flux of atomic hydrogen at the upper boundary and the eddy diffusion coefficient [c.f. *Wallace and Hunten*, 1973]. In fact, the H profile is very insensitive to the eddy coefficient for the low

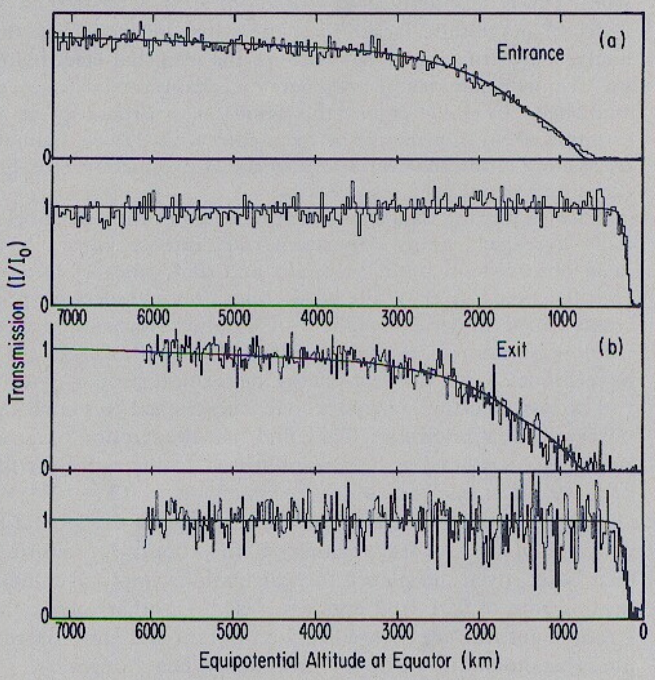

Fig. 11. (*a*) γ Peg entrance and (*b*) exit occultation light curves, model and observed. Two wavelength ranges (top panels: $958 \leq \lambda \leq 1004$, H_2 bands; bottom panels: $1254 \leq \lambda \leq 1356$ Å, H_2 Rayleigh scattering and hydrocarbon absorption) are shown for each case. Exit occultation has been time-reversed to plot on the same altitude scale. Altitudes shown are referred to equatorial latitude as discussed in the text.

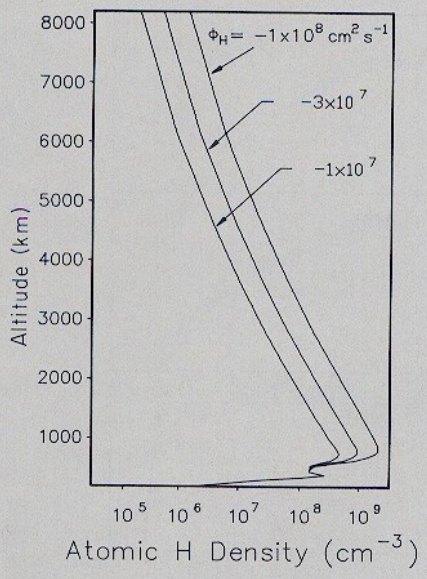

Fig. 12. Theoretical H profiles in an H_2 atmosphere computed assuming various downward H fluxes, ϕ_H. The $\phi_H = -3 \times 10^7$ cm^{-2} s^{-1} case fits the observations best.

levels of eddy mixing present on Uranus. A constant eddy coefficient of 10^3 cm^2 s^{-1} is used in the calculations but a value 10 times larger would only lower the peak H density by ~20%. The bulk of atomic hydrogen is lost through three-body recombination. Hydrocarbon photochemistry is responsible for the secondary peak at low altitudes. The model with $\phi_H = -3 \times 10^7$ cm^2 s^{-1} most closely fits the observations. Previously, *Broadfoot et al.* [1986] estimated the atomic hydrogen production rate from analysis of the electroflow spectrum. The H flux derived by Broadfoot et al. is more than an order of magnitude larger than the value inferred from this analysis. For this and other reasons, the idea that electroglow on Uranus originates in low energy electron impact has been challenged by *Yelle et al.* [this issue]. The Broadfoot et al. estimate could in principle be reconciled with this ϕ_H estimate by assuing latitudinal variations in the H production rate, but the issue has not been resolved.

Auroral heating may also contribute significantly to the globally averaged energy deposition rate. Intense aurora have been observed on both the sunlit and dark sides of Uranus [*Sandel*, 1986]. J. H. Waite et al. (Suprathermal electron processes in the upper atmosphere of Uranus: Aurora and electroglow, submitted to *Journal of Geophysical Research*, 1987) have modeled the auroral energy deposition process with a two-stream electron transport code, constrained to match the observed EUV intensities. They find that the fraction of auroral energy deposited as heat is insensitive to the energy of the primary electrons and is approximately 6 to 12 $\times$ 10^{10} W. (The uncertainty is due to lack of knowledge of the atomic H densities in the auroral regions.) If the energy is uniformly distributed over the planet the calculations imply a column heating rate of 0.01–0.02 ergs cm^{-2} s^{-1}. In other words, the Uranian aurorae are energetically important and may contribute substantially to the upper atmospheric heat budget.

Other processes are capable of heating the upper atmosphere of Uranus. For example, Joule heating may be particularly important on Uranus because of the planet's peculiar rotational properties. The amount of Joule heating depends on the relative velocities between ions and neutrals and on the ionospheric densities. On Uranus the ions are constrained to move along magnetic field lines while the neutral gas is subject to the winds in the upper atmosphere. At the cloud tops the relative velocity between the neutral atmosphere and magnetic field reaches 200 m s^{-1} [*Smith et al.*, 1986]. In the thermosphere it is possible that the wind velocities are much larger. Using a relative velocity of 200 m s^{-1} and the model ionosphere of *Chandler and Waite* [1986] we estimate a Joule heating rate of 2.5 ergs cm^{-2} s^{-1}. However, both the ion-neutral relative velocity and the ionospheric densities are very uncertain and this calculation could easily be in error by several orders of magnitude. Nevertheless, the calculation does indicate that Joule heating is potentially an important source of energy for the upper atmosphere.

4.2. *Extended Hydrogen Exosphere and Gas Drag on Orbiting Particles*

The extended exosphere at Uranus, with its important implications for the evolution of the ring system and as a source of magnetospheric plasma, was one of the major discoveries of the Uranus encounter. This extended exosphere is due to the combination of the high exospheric temperature and the relatively small size of the planet. Augmenting the extended exosphere is a nonthermal H corona inferred from H Ly α emissions detected by the UVS [*Broadfoot et al.*, 1986]. A simplified analysis suggests that this population may contribute even more H density at 2 R_U than does the thermal component, but further analysis is necessary. In order to be conservative therefore the nonthermal contribution is omitted from the following discussion.

The temperature of the exosphere derived from an analysis of the solar occultation in section 2.5 is 800 $\pm$ 100 K. The H scale height and density at 5000 km are ~1000 km and 3 $\times$ 10^6 cm^{-3}. Exospheric profiles calculated under the assumptions of various constant temperatures and hydrostatic equilibrium for the exosphere are shown in Figure 13. The best fit temperature and those representing the uncertainty of the fit (compare Figure 3) are used to extrapolate the density measured at 5000 km altitude to 2 R_U. The profiles are calculated assuming the hydrostatic law, which holds even in the exosphere at altitudes low enough that the orbiting states in the particle phase space comprise a negligible fraction of the total. Charge exchange between the neutral exosphere and

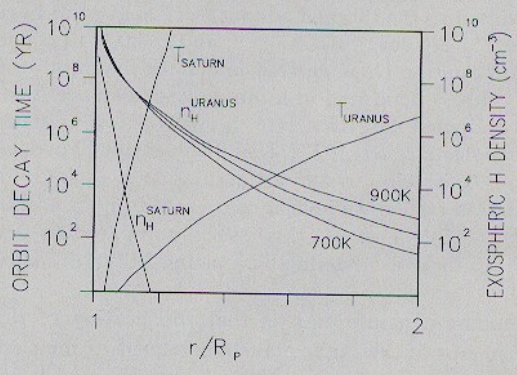

Fig. 13. A comparison of the atomic H exospheric profiles and resulting gas drag lifetimes for particles orbiting Uranus and Saturn. Three Uranian H density profiles as a function of normalized radius r/R_p (R_p is the radius of the planet in question) are shown for differing choices of exospheric temperature. H density profile [*Smith et al.*, 1983] and drag lifetimes derived from it are also shown for Saturn's exosphere. Very different behavior is the result of the higher temperature and lower gravity at Uranus. Lifetimes for orbital decay of a 1-cm orbiting particle are also shown for each planet (using the 800 K profile in the case of Uranus). Drag lifetime of an orbiting particle is proportional to its radius, so the diagram may be used to estimate drag lifetimes for other sizes of particles as well.

ions in the topside ionosphere or magnetospheric plasma may also influence the density distribution in the outer exosphere, but is not included.

An important effect of this part of the exosphere noted by *Broadfoot et al.* [1986] is the drag torque it exerts on the Uranian ring particles. The drag force on an individual particle is given by $c_D A_p m_H n_H v_{rel}^2$, where the dimensionless drag coefficient c_D may be taken as unity, the particle cross sectional area A_p may be taken as πa^2, with a the particle mean radius, and m_H and n_H the H atomic mass and number density, respectively. The relative velocity v_{rel} between the atmosphere and the orbiting particle varies between 0.83 and 0.52 v_0 for 1 $R_U \le r \le 2$ R_U. The local orbital speed is v_0 and an average value of about 0.65 will be assumed for v_{rel}/v_0. Thus the drag force may be approximated by $5 \times 10^{-12} a^2 n_H/r$, with a and n_H in centimeter-gram-second units and r in R_U.

Here we assume an atmospheric H density $n_H = c_1 \exp(c_2/r)$, which is appropriate for an isothermal exosphere with variable gravity but an averaged contribution from centrifugal acceleration. Values of c_1 and c_2 of 4×10^{-5} cm^{-3} and 31 R_U, respectively, were derived for the exospheric temperature of 800 K.

The rate of orbital decay of a ring particle in a circular orbit of radius r, due only to gas drag torque, was calculated by *Broadfoot et al.* [1986] and is given (in R_U/year) by

$$\frac{dr}{dt} = -c_3 \frac{\sqrt{r}}{a} \exp\left(\frac{c_2}{r}\right) \tag{3}$$

where r is measured in R_U and the particle radius a is in centimeters. Although the dimensionless drag coefficient c_D was assumed to be equal to unity, alternative values can be folded into c_3, which otherwise is given by 3×10^{-11} c_1 for a particle density of 1.5 g cm^{-3}. Equation (3) may be integrated analytically in terms of the incomplete gamma function, yielding the time required for orbital evolution between any two radii r_0 and r_1

$$t_1 - t_0 = \frac{a(c_2)^{1/2}}{c_3}\left(\Gamma\left(-\frac{1}{2}, \frac{c_2}{r_0}\right) - \Gamma\left(-\frac{1}{2}, \frac{c_2}{r_1}\right)\right) \tag{4}$$

For large values of x, $\Gamma(-1/2, x) \sim x^{-3/2} e^{-x}(1 - 3/(2x) + 15/(2x)^2 - \cdots)$ [*Abramowitz and Stegun*, 1970]. Figure 13 also shows the orbital decay lifetime as a function of planetocentric distance for 1-cm ring particles as computed using (4). The value assumed for the minimum orbit radius is 1 R_U, but the result is insensitive to the exact value chosen, for reasons that are obvious physically.

The evolution of ring particle orbits is controlled by a number of subtle phenomena besides exospheric drag, as is obvious from the confinement of the bulk of the ring material within a number of very narrow rings. Nevertheless, Figure 13 makes clear that exospheric drag influences the evolution of the ring system. Its influence is strongest for the smallest particles, so exospheric drag offers a convenient explanation for the general lack of small ($a < 1$ cm) particles within the narrow rings that were known before Voyager encounter [see *Tyler et al.*, 1986; *Lane et al.*, 1986; *Holberg et al.*, 1987]. Several implications of the drag torque on the rings are discussed in *Broadfoot et al.* [1986]. One major effect is the relatively short computed orbital lifetimes for some of the rings. For the α, β, and ε rings, where estimates of optical depths and surface mass density were available, Broadfoot et al. estimated orbital lifetimes of 4×10^6, 8×10^6, and 6×10^8 years respectively, based on their collective drag torques. That is, the rings were assumed to evolve as unitary collective entities, which is equivalent to assuming a single particle size. For the 800 K exosphere inferred here, these estimates should be decreased slightly. However, these estimates apply only to isolated rings and do not include the angular momentum contributed by possible shepherding satellites, which are believed to confine the rings.

As an example of the influence of shepherds it is useful to consider the ε rings. It is now known that the ε ring is confined by orbital resonances involving 1986U7 and 1986U8 [*Porco and Goldreich*, 1987; *French et al.*, 1983]. These two satellites and the ε ring thus form a system which evolves quasistatically with approximately 25 times the orbital angular momentum of the ε ring itself. The drag lifetime of the ε ring can thus be increased proportionately, to a value in excess of the age of the solar system. *Goldreich and Porco* [1987] have further compared the exospheric drag torque on the ε ring with the satellite torques and generally find that the drag torque does not exceed the confining satellite torques. This is not the case however for the α and β rings where Goldreich and Porco find the drag torque exceeds the shepherding torque due to hypothesized satellites by nearly two orders of magnetude. Thus the inferred drag torque leads to difficulties in understanding both the orbital lifetime and the confinement of these two inner rings.

However, the stabilizing effect of shepherds on the Uranian rings is clear; unprotected small ring particles should rapidly disappear. Thus the sparse population of the Uranian ring system may be the result of a natural selection for particles in orbits that happen to be protected against angular momentum loss. In this view, the remarkable appearance of the Uranian rings may be attributable to thermospheric drag. Although this idea is rather speculative, one possible test is the Neptunian ring system, which apparently also consists of a few isolated components [*Hubbard et al.*, 1986]. Discovery that Neptune possesses a Uranus-like extensive thermosphere would be consistent with the hypothesis of drag-induced sparsity.

Another likely consequence of exospheric drag is a steady flux of inwardly drifting small particles derived from the narrow optically thick rings and possible small satellites between the rings. *Broadfoot et al.* [1986] noted that the complex of broad tenous interring material seen in the high phase angle image of the rings [*Smith et al.*, 1986] might represent a steady state flux of such fine particles. It is known from occultation data [*Holberg et al.*, 1987] that the visible portions of the new ring, 1986U1R, are composed of very small ($\sim$1 mm) particles. In the presence of exospheric drag the lifetime of such a ring is very short ($\ll$1000 years). The fine material in this ring is presumably derived from an unseen ($<$10 km) body or bodies in the orbit of 1986U1R.

Considering the effects of gas drag on individual particles within a ring suggests that there might be a minimum size for the ring particles which can be protected from orbital decay due to atmospheric drag, if the particle size-dependent gas drag torque can drive relative radial diffusion of different-sized ring particles. If the torque per unit ring particle mass is given by $dl/dt = (GM_S r/v_0 x^2)^2$ [*Goldreich and Tremaine*, 1979] for shepherd (mass M_S and radius R_S) and ring particle orbit separation x down to some minimum value αR_S, declining thereafter (due, for example, to breakdown of the shepherding model), then the minimum mass ring particles will be those whose orbits decay to and just stop at this critical separation. Taking the sum of the drag and shepherding torques to be zero yields, after some algebra and simplifying assumptions (such as similar densities for shepherd and Uranus), that the minimum particle size in cm is very roughly 10^{-15} $(R_U/R_S)^2 \alpha^4/r^3$ n_H (here again, r is measured in R_U). Taking as

an example $\alpha = r = 2$, this gives a minimum particle radius on the order of 1 μ for a 2 km shepherd and 10 μ for a 0.5 km shepherd. The result of such a calculation is too dependent on the unknown value of α to be closer than an order-of-magnitude estimate, however.

In a similar way gas drag might drive orbiting particles down against the shepherding torque from an inner, larger (and hence less influenced by gas drag) satellite. This combination of localized barrier and inward diffusion could form a narrow ring without involving an outer shepherd. However, a narrow ring formed in this way would not have sharp inner or outer boundaries as do the classical rings.

4.3. *Hydrocarbons: Chemistry and Transport*

4.3.1. *Photochemistry.* The photochemistry of methane on the major planets has been developed since the early 1970s by several authors [e.g., *Strobel*, 1973; *Atreya et al.*, 1981; *Gladstone*, 1982; *Yung et al.*, 1984; *Atreya*, 1984, 1986; and *Romani*, 1986]. For the latest information on the relevant rate constants and the cross sections, the reader is referred to *Yung et al.* [1984] and *Atreya* [1986, pp. 98–105]. Here, we present only a brief outline of the CH_4 photochemistry. The absorption of solar photons of wavelength $\lambda \leq 1450$ Å by CH_4 results in the production of $^1CH_2$, $^3CH_2$, and CH. (For all practical purposes, however, the CH_4 photolysis takes place at the wavelength of 1216 Å because of the large flux of solar H Ly α photons). The $^1CH_2$ radicals react with H_2 to form methyl radicals (CH_3) which, in turn, react with $^3CH_2$ to yield ethylene, C_2H_4. CH radicals also form C_2H_4 on reaction with CH_4. Photolysis of C_2H_4 proceeds primarily at wavelengths ≥ 1400 Å, resulting in the formation of acetylene, C_2H_2. Chemical reactions of C_2H_4 in the presence of H and H_2 recycle some of the CH_4. C_2H_2 and C_2H_4 are also produced following the photolysis of ethane, C_2H_6, at wavelengths $\leq$ 1600 Å. C_2H_6 itself is produced on the self-reaction of the methyl radicals. C_2H_2, C_2H_4, and C_2H_6 are stable hydrocarbon products of the CH_4 photochemistry. Photolysis of C_2H_2 is likely, and subsequent chemistry can result in the formation of diacetylene, C_4H_2, and perhaps even higher order polyacetylenes.

The low temperatures and weak vertical mixing on Uranus lead to some interesting differences between photochemistry on that planet and photochemistry on Jupiter and Saturn. Because of the relatively low temperatures encountered in the lower stratosphere, C_2H_2 and C_2H_6 are expected to condense and form hazes at pressures of 5–10 mbars [*Romani*, 1986]. In addition C_4H_2 would condense at $\sim$0.1 mbar, if it were sufficiently abundant. *Pollack et al.* [this issue] discuss such high-altitude hazes further. Since the UV opacity due to the condensed phase hydrocarbons on Uranus is negligible, the transmission characteristics recorded in the occultation experiment are attributed to the atmospheric constituents in the gas phase. Among the hydrocarbons only CH_4, C_2H_2, and C_2H_6 are expected to have large enough gas phase abundances on Uranus to influence the transmission characteristics.

In order to explore the consequences of the atmospheric distributions determined by the UVS, a basic one-dimensional photochemical model incorporating the chemistry described previously was solved numerically to yield height distributions of all the hydrocarbon products [*Romani*, 1986]. The resulting distributions depend on the atmospheric thermal profile and a model of the variation of the eddy diffusion coefficient with density (see section 4.3.2). The tropopause temperature is assumed to be 52 K at a level of 100 mbar on the basis of Voyager IRIS measurements [*Hanel et al.*, 1986]. The tropopause (or cold-trap) temperature is assumed to fix the mixing ratio of CH_4 to its saturation value (i.e., 8.5×10^{-5} or 10^{15} cm^{-3} [*Atreya*, 1986]) at that level. However, even the low vapor phase CH_4 abundance at the extremely low cold trap temperature at Uranus is large enough to produce an H Ly α vertical optical depth of $n_{CH_4}\,\sigma_{CH_4}$ (1216 Å)H $> 10^4$ in the absence of photolysis. This implies that most of the CH_4 photolysis occurs far above the tropopause (i.e., where unit optical depth is reached).

As is discussed by *Yelle et al.* [1987], proximity between the condensation and photochemical regions could affect the hydrocarbon distributions. The importance of Rayleigh scattering in the occultation data and the detection of Raman scattered Ly α emissions [*Broadfoot et al.*, 1986; *Yelle et al.*, 1987] imply that multiple scattering of solar UV may alter the photodissociation rates. Both of these effects are negligible in the methane photochemistry on Jupiter and Saturn and are unimportant on Uranus if the eddy diffusion model assumed here ($K_h = 10^4$ cm^2 s^{-1}, $K \propto n_a^{-1/2}$; see section 4.3.2) is correct. If eddy diffusion is much slower than in this model, however, then these effects must be considered.

4.3.2. *Constraints on eddy diffusion.* The distribution of photochemically active species in an atmosphere depends critically on the strength of vertical mixing which is generally expressed in terms of a phenomenological height-dependent eddy diffusion coefficient, $K(z)$ [c.f. *Colegrove et al.*, 1965; *Hunten*, 1975]. The competition between eddy and molecular diffusion determines the altitude range where diffusive separation becomes important, i.e., the location of the homopause. For stability of a species which is photochemically or chemically destroyed at high altitudes there must be replenishment by flow from lower altitudes. The efficiency of this transport at each level is expressed in terms of the value of the eddy diffusion coefficient there.

Since $K(z)$ is a phenomenologically determined function, it is customarily specified by giving its value K_h at the homopause and assuming a particular functional form. Since the homopause is, by definition, the altitude where the eddy and (calculable) molecular diffusion coefficients are equal, the homopause location is fixed thereby. The functional form of $K(z)$ is generally assumed to be the ambient gas density raised to a constant power.

Generally, both photochemistry and transport are important in determining the altitude profile of methane on the outer planets, and numerical models are required to calculate the methane distribution. The value of K_h is treated as a free parameter in these calculations and is determined by comparison of the models to the observed methane distribution. This method has been applied successfully to the UVS occultation data from Jupiter [*Atreya et al.*, 1981], Saturn [*Atreya*, 1982; *Smith et al.*, 1983], and Titan [*Smith et al.*, 1982]. At Uranus, on the other hand, the density distribution of CH_4 cannot be determined directly from the UVS occultation experiments because its absorption signature is partially masked by Rayleigh scattering of H_2. However, C_2H_2, which is a photochemical product of CH_4, is observed. Through comparison of the photochemical models with the observed C_2H_2 density we can constrain the eddy diffusion coefficient but the analysis turns out to be much more model dependent than was the case for Jupter, Saturn, or Titan. Other methods for determining the eddy diffusion coefficient on major planets, such as the dependence on K_h of the planetary H Ly α and He 584 Å intensities [*Sandel et al.*, 1982], are not appropriate for Uranus because of the effects of electroglow and the low He 584 Å intensity [*Broadfoot et al.*, 1986].

The choice of eddy diffusion model has a dramatic effect on the photochemical profiles of the hydrocarbons on Uranus, as is evident in Figure 14, which shows the variation of CH_4 (top), C_2H_2 (middle), and C_2H_6 (bottom) mixing ratios with differing values of K_h. The importance of photodissociation of CH_4 is evident from the differences between the homopause levels (shown on right ordinate in Figure 14) and the altitudes where H Ly α photolysis diminishes the CH_4 mixing ratio relative to its tropopause value. This difference in altitude is more than 100 km for the $K_h = 10^4$ cm^2 s^{-1} case. The reason for this behavior is that photodissociation is faster than upward diffusion; the (globally averaged) lifetime against photodissociation at the H Ly α unit optical depth level is around 2×10^8 s, while the characteristic time H^2K for eddy diffusion is about 2.5×10^9 s for an eddy diffusion coefficient value K of 10^4 cm^2 s^{-1} and a scale height H of 50 km.

The long wavelength solar occultation light curves were simulated using the model hydrocarbon distributions (CH_4, C_2H_6, and C_2H_2) corresponding to $K_h = 10^7$, 10^5 and 10^4 cm^2 s^{-1} and $K \propto n_a^{-1/2}$ below the homopause, n_a being the ambient atmospheric number density. The $K \propto n_a^{-1/2}$ variation is often assumed but is not necessarily optimal. This dependence of the eddy diffusion coefficient on the atmospheric density has been approximately verified in regions of the Earth's atmosphere [*Hunten*, 1975] and led to consistent models for Jupiter [*Atreya et al.*, 1981] and Saturn [*Atreya*, 1982]. However, constant K models have also been used successfully at Saturn [*Smith et al.*, 1983] and an exponent of $-2/3$ led to good results in models of Titan [*Smith et al.*, 1982]. Since the eddy diffusion concept is a phenomenological model whose extrapolation properties are poorly understood, differences among these values of the exponent are probably not significant. Our observations essentially constrain a complicated average of the values of K over the region below the homopause, and so there are probably a number of combinations of K_h and the exponent of n_a that will fit the observations. Further study combining the occultation measurements with the solar reflection data may allow refinement of our $K(z)$ profile estimate.

The model and observed light curves are compared in Figure 15. The dotted curves show the opacity due to H_2 Rayleigh scattering alone, with the model H_2 profile adjusted to match the observed light curve in Figure 15*c*. Figure 15*c* shows a comparison of model and observed light curves in the $1586 \leq \lambda \leq 1623$ Å region, which is dominated by Rayleigh scattering in H_2. The match in this region indicates that H_2 Rayleigh scattering is being well accounted for in the models, so that Figures 15*a* and 15*b* can be directly interpreted in terms of hydrocarbon abundances. However, in Figures 15*a* and 15*b* the measured opacity at each altitude is greater than expected from Rayleigh scattering alone. Here we interpret this additional opacity in terms of hydrocarbon abundances. Figure 15*a* shows the wavelength interval $1260 \leq \lambda \leq 1352$ Å, where CH_4, C_2H_6 and C_2H_2 all absorb strongly. Because of the difficulty in separating the relative contributions of these species as well as the scattered light problem discussed in section 2.1, this wavelength region essentially establishes an upper limit for the vertical distribution of these hydrocarbons and hence represents an upper bound on the eddy mixing. Figure 15*b* shows the light curve for $1475 \leq \lambda \leq 1575$ Å, a wavelength interval typically dominated by a very strong pair of C_2H_2 absorption features. In section 2.6 the presence of C_2H_2 was tentatively inferred from the shape of the I/I_0 spectrum in this wavelength region at an altitude roughly corresponding to the half-light point in Figure 15*b*. Further, the C_2H_2 mixing ratio deduced from this spectrum is consistent with that of the photochemical model used to compute the model I/I_0 light curve in Figure 15*b*. Consequently, we interpret the light curves in Figure 15*b* as constraining the C_2H_2 mixing ratio. The closeness in fit between the $K_h = 10^4$ cm^2

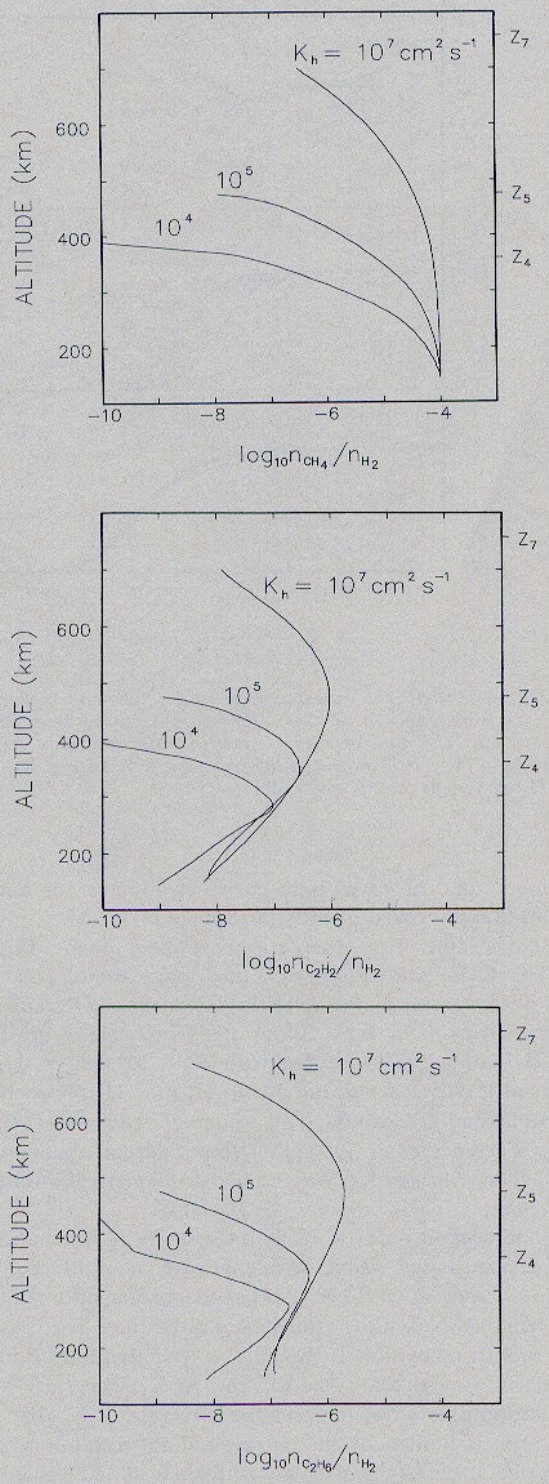

Fig. 14. Photochemical models of hydrocarbon distribution parameterized by K_h, the homopause value for the eddy diffusion coefficient. (Top) CH_4 profiles. (Middle) C_2H_2 profiles. and (Bottom) C_2H_6 profiles. Model altitude scale has been adjusted to fit the observed n_{H_2} distribution. Homopause altitudes z_n are plotted at right for $K_h = 10^n$ cm^2 s^{-1}.

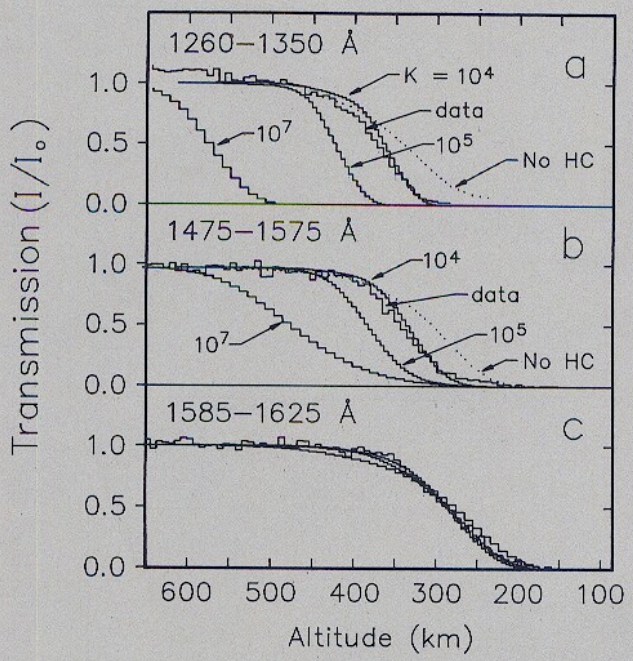

Fig. 15. Model light curves computed for the models shown in Figure 14, superimposed on the observed light curves. Best fit is for $K_h = 10^4$ cm^2 s^{-1}. Dotted curves show the effects of pure Rayleigh scattering in H_2, with no hydrocarbon absorption. In Figure 15*c* the pure H_2 curve falls on top of the other curves.

s^{-1} model and observed light curves in Figures 15*a* and 15*b* implies that low levels of eddy mixing are preferred.

There is some prior observational support for low values of K_h. The C_2H_2 absorption signature longward of 1600 Å in IUE observations of the reflection spectrum of Uranus was interpreted to yield $K_h = 10^5$ or 10^6 [*Encrenaz et al.*, 1986]. The IUE data are consistent with $K_h = 10^4$ cm^2 s^{-1} if the effects of Rayleigh scattering due to H_2 on CH_4 photochemistry are taken into account. This source of opacity was neglected by *Encrenez et al.* [1986] so that a larger abundance of C_2H_2 (hence larger K_h) was needed to explain the observed absorption.

In addition, in order to explain the intensity fluctuations in their ground-based visible-wavelength stellar occultation light curves, *French et al.* [1983] proposed propagation of short wavelength waves in the atmosphere of Uranus. They asserted that such propagation is possible only if the eddy diffusion coefficient is less than 3×10^4 cm^2 s^{-1}. Since their stellar occultation data cover the pressure interval 0.3–30 μbar, their constraint is limited by the corresponding uncertainty in the atmospheric density associated with their stated value of K. Nevertheless, since the molecular diffusion coefficient varies through the range 5×10^3 to 5×10^5 cm^2 s^{-1} over this interval, their constraint is consistent with $K_h = 10^4$ cm^2 s^{-1}.

There also exists some evidence for an even smaller value of K_h. *Yelle et al.* [1987] have inferred an eddy diffusion coefficient in the range 100–350 cm^2 s^{-1} in the region between 500 μbar and 100 mbar from analysis of the Raman scattered H Ly α line observed by the UVS. The presence of the Raman scattered H Ly α line implies that the vertical 1216 Å optical depth above 500 μbar must be small. This implies hydrocarbon concentrations (especially CH_4) near 500 μbar smaller than predicted by the $K_h = 10^4$ cm^2 s^{-1} photochemical model if the $K \propto n_a^{-1/2}$ extrapolation is assumed.

One possible explanation for these differences between the hydrocarbon distributions derived from the two analyses could conceivably be substantial latitudinal variations in the hydrocarbon abundances. The Raman line analyzed by *Yelle et al.* [1987] was observed near the subsolar point (close to the IAU south pole) while the solar occultation, of course, occurred near the terminator (at $\simeq -4°$ latitude). Although the H_2 and temperature profiles were found in section 3.3 to be nearly independent of latitude (if corrected for planetary oblateness), the observations demonstrating this uniformity for H_2 do not similarly constrain the hydrocarbon abundances. Latitudinal variations in hydrocarbon profiles could be caused by variations in the amount of vertical mixing and are expected on the basis of photochemical effects as well.

It should also be noted that even the solar occultation measurement does not by itself necessarily imply large vertical H Ly α optical depths above the 500 μbar level. Only C_2H_2 is definitely detected with a tangential column abundance of 6×10^{15} cm^{-2} near the 40 μbar level. If the atmosphere is diffusively separated there, C_2H_2 will have a scale height of about 4 km, and the vertical optical depth at H Ly α above 500 μbar will be $\gg 1$. However, if C_2H_2 is fully mixed the scale height will be about 50 km. Extrapolation from 40 to 500 μbar using this scale height predicts a density at 500 μbar of 3×10^8 cm^{-3} and a vertical optical depth due solely to C_2H_2 at H Ly α of 0.04. The reason for the apparent conflict between the occultation and reflectance estimates of optical depth at 1216 Å is that the photochemical models predict that the concentration of C_2H_2 detected by the UVS will be accompanied by much larger concentrations of CH_4.

The question of the CH_4 abundance is to some extent dependent on the details of the observation. In section 2.6 an upper limit of 10^{-7} was found for the mixing ratio of fully mixed CH_4. However, in the photochemical models introduced in the current section the mixing ratio of CH_4 in the best fitting ($K_h = 10^4$ cm^2 s^{-1}) of the models which were tried varies from 10^{-6} to essentially zero over the measurement interval. As can be seen from Figure 14 the value of n_{CH_4}/n_{H_2} in these photochemical models varies very rapidly with altitude down to about the 250 km level, below which point the value of 10^{-4} is asymptotically reached. Consequently, different measurements of n_{CH_4}/n_{H_2} are likely to give widely varying results depending on their mean altitude of measurement. For example, measurements of Uranus' thermal emission spectrum in the far infrared [*Orton et al.*, 1986] and imaging measurements of aerosols by Voyager 2 [*Pollack et al.*, this issue] indicate a possibly higher upper limit for the CH_4 abundance than found here [*Appleby*, 1986], but this is probably because these measurements are sensitive to CH_4 at lower altitudes than those probed by the UVS occultation. Although in prior Voyager observations (Jupiter, Saturn, Titan) the critical levels for hydrocarbon measurements (e.g., near the homopause) fell nicely within the UVS occultation altitude range, at Uranus the hydrocarbons are so low in abundance that the critical measurement range falls between the various instruments' optimum altitudes.

4.3.3. *Comparison with Jupiter and Saturn.* It is of interest to compare the limits placed on the eddy diffusion coefficient on Uranus to the values determined for Saturn and Jupiter. The value of K_h on Jupiter, inferred from the UVS stellar occulation, is $\sim 10^6$ cm^2 s^{-1} near the 1 μbar level [*Atreya et al.*, 1981]. Deeper in the atmosphere, near the 100 mbar level, the eddy coefficient is inferred to be 1×10^4 cm^2 s^{-1} from analysis of the NH_3 abundance [*Kaye and Strobel*, 1983].

Similar values are also required by *Massie and Hunten* [1982] to explain the orthopara ratio in H_2. On Saturn, analysis of the UVS stellar occultation implied an eddy coefficient of 2×10^8 cm^2 s^{-1} near 10^{-3} μbar [*Atreya*, 1982]. A separate analysis by *Smith et al.* [1983], however, determined a value of 5×10^6 cm^2 s^{-1}. Analysis of the He 584 Å resonance line also implied high values of K_h, on the order of 10^8 cm^2 s^{-1} [*Sandel et al.*, 1982]. The eddy diffusion coefficient deep in the Saturnian atmosphere (near 100 mbar) appears to be $\sim 10^4$ cm^2 s^{-1} [*Kaye and Strobel*, 1984]. Thus the eddy diffusion coefficients inferred for Jupiter and Saturn both at the 100-mbar level and above the μbar level appear to be much larger than at comparable pressures in the Uranian atmosphere.

Unfortunately, our knowledge of the processes responsible for eddy diffusion is too primitive to permit confident interpretation of the low values of K in terms of atmospheric dynamics. Current ideas about eddy diffusion suggest that it could be the result of atmospheric wave motion and/or vertical components of largely horizontal winds. Thus the low eddy diffusion coefficient on Uranus may suggest that the magnitudes of atmospheric waves and/or high-altitude winds may be smaller at Uranus. Small atmospheric motions at Uranus may be the result of the lack of an internal heat source or the presently insignificant diurnal heating variation. It is also conceivable that what eddy diffusion there is at Uranus may be by default the result of some mechanism that is negligible on other planets.

5. Conclusions

Figure 16 summarizes the inferences of previous sections regarding temperature and density profiles. This figure is an elaboration of Figure 4, with extrapolated and interpolated profiles and the inclusion of the $K_h = 10^4$ cm^2 s^{-1} photochemistry model. Also, the abundance of helium (not measured in this work but included for completeness) is indicated; below 500 km altitude the 15% mixing ratio found by *Hanel et al.* [1986] is assumed and above 500 m diffusive separation following the indicated $T(z)$ is assumed. This figure represents our conclusions, summarized below, based on the measurements shown in Figure 4.

The atmosphere of Uranus above about the 1-mbar level is much clearer at EUV wavelengths than the previously visited gas giant planets because its H-H_2-He atmosphere has very little contamination with absorbing or aerosol-precipitating species such as CH_4, C_2H_2, NH_3, etc. The average methane mixing ratio n_{CH_4}/n_{H_2} is $\leq 10^{-7}$ over the altitude range 200–400 km (relative to r = 25,550 km at the equator). Other hydrocarbons are even less abundant, with $n_{C_2H_2}/n_{H_2} \simeq 10^{-8}$ and $n_{C_2H_6}/n_{H_2} \leq$ several $\times 10^{-8}$. This appears to be the result of a number of factors possibly including: tropospheric depletions, low stratospheric temperatures and a low rate of vertical mixing. Because the upper atmosphere is so clear, Rayleigh scattering by H_2 is the major source of opacity longward of H Ly α and thus we are able to determine the H_2 profile over a very wide pressure range.

Conversely, determination of the hydrocarbon profiles is made difficult by the low hydrocarbon mixing ratios. As is discussed in sections 2.6 and 4.3, the only hydrocarbon spectral signature that is directly observed in the data is that of C_2H_2, although there are indications of the presence of other species. As a substitute for direct measurement of other hydrocarbon abundances, photochemical models were constructed and compared with the occultation observations. These models assumed an eddy diffusion coefficient given by $K(z) = K_h[n_a(z_h)/n_a(z)]^\alpha$ with n_a the ambient gas density and the subscript h denoting homopause values. With the assumption of $\alpha = 1/2$ a reasonable fit was found for $K_h = 10^4$ cm^2 s^{-1} but other combinations of α and K_h or other functional forms may be found that fit equally well. However, because of the low hydrocarbon abundances we do not probe the homopause region directly and thus our estimate for K_h is more model dependent than in prior work for Jupiter and Saturn.

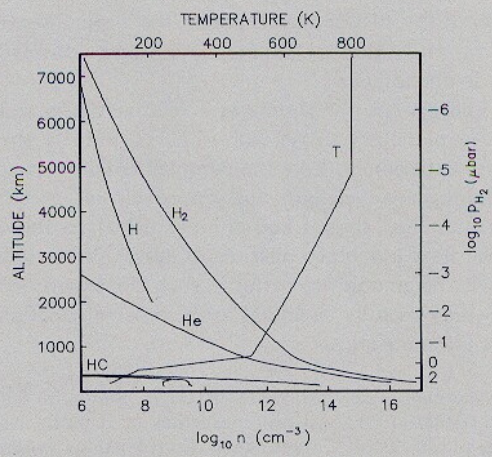

Fig. 16. Abundance and temperature profiles inferred from the observations. Each curve is labeled with its associated variable except the hydrocarbons (HC). Hydrocarbons are, in order of increasing abundance, C_2H_2, C_2H_6, and CH_4. H_2 partial pressure (p_{H_2}) is shown at right. Helium was not detectable in the occultations, and so has been extrapolated upwards from the IRIS measurements [*Hanel et al.*, 1986].

Other estimates of eddy mixing based on the solar reflection spectrum [*Yelle et al.*, 1987] indicate an even lower level of eddy mixing than the photochemical model fits do. This difference may be related to the difficulty in determining $K(z)$ or may be due to a falloff in mixing toward the poles (where the *Yelle et al.* [1987] estimate was derived). In either case it seems clear that the strength of eddy mixing on Uranus is much weaker than at comparable levels in the atmospheres of Jupiter or Saturn.

The temperature rises rapidly over the 1- to 0.1-μbar region, eventually leveling out near a temperature of 800 K. The similarity of the temperature profiles on the day and night sides may be a consequence of efficient lateral transport or may indicate that the source of upper atmospheric heating is planet wide. The high degree of horizonal thermal uniformity contrasts with the low degree of vertical mixing of the hydrocarbon distributions. If the low rate of vertical transport implies a low rate of horizonal transport, the horizonal thermal uniformity might then be the result of a global thermospheric heat source.

The high temperature and the abundance of atomic hydrogen imply an unusually extensive exosphere. This great extension implies a significant drag force on even meter-sized particles orbiting in the ring system, suggesting either a recent formation epoch or the presence of large stabilizing torques. As is discussed in section 4.2 even the visual appearance of the ring system may be dominated by gas drag. The thermal H exospheric component may be augmented by the even more extensive nonthermal H corona observed out to about 4 R_U by *Broadfoot et al.* [1986]. These two H distributions clearly will also interact strongly with the magnetospheric charged particle populations. Thus the Uranian thermosphere may be

seen to blur the distinction between the domains normally associated with purely atmospheric and purely magnetospheric phenomena.

These findings are the results of a relatively new technique for probing planetary upper atmospheres, namely the EUV occultation experiment. Like the complementary related techniques at longer wavelength, this approach has great power and an unmatched spatial and compositional resolution. Although the next planetary missions (Galileo, Mars Observer, CRAF) will be unable to perform such an experiment, this capability may usefully be added to the repertoires of missions still in the planning stages.

Acknowledgments. The assistance of G. R. Smith in the application of occultation analysis procedures has been indispensible for this work and is greatly appreciated. Conversations with D. M. Hunten, who originally suggested the importance of atmospheric gas drag on the rings, have likewise been very helpful. We thank R. Greenberg and C. C. Porco for useful discussion of ring dynamics and J. C. McConnell for helpful editorial suggestions. This work was supported by NASA grant NAGW-610 and by a subcontract under NASA contract NAS7-918. S. K. Atreya acknowledges support received from NASA Planetary Atmospheres Program Grant NSG 7404, and P. Romani acknowledges the NAS/NRC Resident Research program for support at NASA Goddard Space Flight Center.

The Editor thanks J. A. Kaye and another referee for their assistance in evaluating this paper.

REFERENCES

Abramowitz, M., and I. A. Stegun, *Handbook of Mathematical Functions*, National Bureau of Standards, Washington, D. C., 1970.

Appleby, J. F., Radiative-convective models of Uranus and Neptune, *Icarus*, *65*, 383, 1986.

Atreya, S. K., Eddy mixing coefficient on Saturn, *Planet. Space Sci.*, *30*, 849, 1982.

Atreya, S. K., Aeronomy, Uranus and Neptune, *NASA Conf. Publ.*, *CP-2330*, 55, 1984.

Atreya, S. K., *Atmospheres and Ionospheres of the Outer Planets and Their Satellites*, Springer-Verlag, New York, 1986.

Atreya, S. K., T. M. Donahue, B. R. Sandel, A. L. Broadfoot, and G. R. Smith, Jovian upper atmospheric temperature measurement by the Voyager 1 UV spectrometer, *Geophys. Res. Lett.*, *6*, 795, 1979.

Atreya, S. K., T. M. Donahue, and M. C. Festou, Jupiter: Structure and composition of the upper atmosphere, *Astrophys. J.*, *247*, L43, 1981.

Broadfoot, A. L., et al., Ultraviolet spectrometer experiment for the Voyager mission, *Space Sci. Rev.*, *21*, 183, 1977.

Broadfoot, A. L., et al., Ultraviolet spectrometer observations of Uranus, *Science*, *233*, 74, 1986.

Caldwell, J., T. Owen, A. R. Rivolo, V. Moore, G. E. Hunt, and P. S. Butterworth, Observations of Uranus, Neptune, and Titan by the International Ultraviolet Explorer, *Astron. J.*, *86*, 298, 1981.

Chamberlain, J. W., Planetary coronae and atmospheric evaporation, *Planet. Space Sci.*, *11*, 901, 1963.

Chandler, M. O., and J. H. Waite, Jr., The ionosphere of Uranus: A myriad of possibilities, *Geophys. Res. Lett.*, *13*, 6, 1986.

Clarke, J., S. Durrance, S. Atreya, A. Barnes, J. Belcher, M. Festou, C. Imhoff, J. Mihalov, W. Moos, J. Murthy, A. Pradhan, and T. Skinner, Continued observations of the H Ly-alpha emission from Uranus, *J. Geophys. Res.*, *91*, 8771, 1986.

Colegrove, F. D., W. B. Hanson, and F. S. Johnson, Eddy diffusion and oxygen transport in the lower thermosphere, *J. Geophys. Res.*, *70*, 4931, 1965.

Elliot, J. L., R. G. French, J. A. Frogel, J. H. Elias, D. J. Mink, and W. Liller, Orbits of nine Uranian rings, *Astron. J.*, *86*, 444, 1981.

Encrenaz, T., M. Combes, S. Atreya, P. Romani, K. Fricke, V. Moore, G. Hunt, R. Wagener, T. Owen, J. Caldwell, and P. Butterworth, A study of the upper atmosphere of Uranus using IUE, *Astron. Astrophys.*, *162*, 317, 1986.

Festou, M. C., and S. K. Atreya, Voyager ultraviolet stellar occultation measurements of the composition and thermal profiles of the Saturnian upper atmosphere, *Geophys. Res. Lett.*, *9*, 1147, 1982.

Festou, M. C., S. K. Atreya, T. M. Donahue, B. R. Sandel, D. E. Shemansky, and A. L. Broadfoot, Composition and thermal profiles of the Jovian upper atmosphere determined by the Voyager ultraviolet stellar occultation experiment, *J. Geophys. Res.*, *86*, 5715, 1981.

French, R. G., J. L. Elliot, E. W. Dunham, D. A. Allen, J. H. Elias, J. A. Frogel, and W. Liller, The thermal structure and energy balance of the Uranian upper atmosphere, *Icarus*, *53*, 399, 1983.

Gladstone, G. R., Radiative transfer and photochemistry in the upper atmosphere of Jupiter, Ph.D. thesis, Calif. Inst. of Technol., Pasadena, 1982.

Goldreich, P., and C. C. Porco, Shepherding of the Uranian rings, II, Dynamics, *Astrophys. J.*, *93*, 730, 1987.

Goldreich, P., and S. Tremaine, Towards a theory for the Uranian rings, *Nature*, *277*, 97, 1979.

Hanel, R., et al., Infrared observations of the Uranian system, *Science*, *233*, 70, 1986.

Hanley, H. J. M., R. D. McCarthy, and H. Inteman, The viscosity and thermal conductivity of dilute gaseous hydrogen from 15 to 5000 K, *J. Res. Natl. Bur. Stand., Sect. A.*, *74*, 331, 1970.

Holberg, J. B., P. D. Nicholson, R. G. French, and J. L. Elliot, Stellar occultation probes of the Uranian rings at 0.1 and 2.2 μm: A comparison of Voyager UVS and Earth-based results, *Astron. J.*, *94*, 178, 1987.

Hubbard, W. B., A Brahic, B. Sicardy, L.-R. Elicer, F. Roques, and F. Vilas, Occultation detection of a Neptunian ring-like arc, *Nature*, *319*, 626, 1986.

Hunten, D. M., Vertical transport in atmospheres, in *Atmospheres of Earth and the Planets*, edited by B. M. McCormac, p. 59, D. Reidel, Hingham, Mass., 1975.

Hunten, D. M., and A. J. Dessler, Soft electrons as a possible heat source for Jupiter's thermosphere, *Planet. Space Sci.*, *25*, 817, 1977.

Kaye, J. A., and D. F. Strobel, HCN formation on Jupiter, The coupled photochemistry of ammonia and acetylene, *Icarus*, *54*, 417, 1983.

Kaye, J. A., and D. F. Strobel, Phosphine photochemistry in the atmosphere of Saturn, *Icarus*, *59*, 314, 1984.

Lane, A. L., et al., Photometry from Voyager 2: Initial results from the Uranian atmosphere, satellites, and rings, *Science*, *233*, 65, 1986.

Lindal, G. F., J. R. Lyons, D. N. Sweetnam, V. R. Eshleman, D. P. Hinson, and G. L. Tyler, The atmosphere of Uranus: Results of the Voyager 2 radio occultation measurements, *Bull. Am. Astron. Soc.*, *18*, 756, 1986.

Massie, S. T., and D. M. Hunten, Conversion of para and ortho hydrogen in the Jovian planets, *Icarus*, *49*, 213, 1982.

Orton, G. S., A. T. Tokunaga, and J. Caldwell, Observational constraints on the atmospheres of Uranus and Neptune from new measurements near 10 μm, *Icarus*, *56*, 147, 1983.

Orton, G. S., M. J. Griffin, P. A. R. Ade, I. G. Nolt, J. V. Radostitz, E. I. Robson, and W. K. Gear, Submillimeter and millimeter observations of Uranus and Neptune, *Icarus*, *67*, 289, 1986.

Pollack, J. B., K. Rages, S. Pope, M. Tomasko, P. N. Romani, and S. K. Atreya, Nature of the stratospheric haze on Uranus: Evidence for condensed hydrocarbons, *J. Geophys. Res.*, this issue.

Porco, C. C., and P. Goldreich, Shepherding of the Uranian rings, I, Kinematics, *Astrophys. J.*, *93*, 724, 1987.

Romani, P. N., Clouds and methane photochemical hazes on the outer planets, Ph.D. thesis, Univ. of Mich., Ann Arbor, 1986.

Sandel, B. R., Coupling of the atmosphere and magnetosphere: UVS observations of Uranus, paper presented at the Second Neil Brice Symposium on the Magnetosphere of the Outer Planets, Univ. of Iowa, Iowa City, Iowa, 1986.

Sandel, B. R., and A. L. Broadfoot, Statistical performance of the intensified charge coupled device, *Appl. Opt.*, *25*, 4135, 1986.

Sandel, B. R., J. C. McConnell, and D. F. Strobel, Eddy diffusion at Saturn's homopause, *Geophys. Res. Lett.*, *9*, 1077, 1982.

Savage, B. D., W. D. Cochran, and P. R. Wesselius, Ultraviolet albedos of Uranus and Neptune, *Astrophys. J.*, *237*, 627, 1980.

Shemansky, D. E., and G. R. Smith, The implication for the presence of a magnetosphere on Uranus in the relationship of EUV and radio emission, *Geophys. Res. Lett.*, *13*, 2, 1986.

Sicardy, B., M. Combes, J. Lecacheux, P. Bouchet, A. Brahic, P. Laques, C. Perrier, L. Vapillon, and Y. Zeau, Variations of the stratospheric temperature along the limb of Uranus: Results of the 22 April 1982 stellar occultation, *Icarus*, *64*, 88, 1985.

Smith, B. A., et al., Voyager 2 in the Uranian system: Imaging science results, *Science*, *233*, 43, 1986.

Smith, G. R., D. F. Strobel, A. L. Broadfoot, B. R. Sandel, D. E. Shemansky, and J. B. Holberg, Titan's upper atmosphere: Composition and temperature from the EUV solar occultation results, *J. Geophys. Res.*, *87*, 1351, 1982.

Smith, G. R., D. E. Shemansky, J. B. Holberg, A. L. Broadfoot, B. R. Sandel, and J. C. McConnell, Saturn's upper atmosphere from the

Voyager 2 EUV solar and stellar occultations, *J. Geophys. Res.*, *88*, 8667, 1983.

Stone, E. C., and E. D. Miner, The Voyager 2 encounter with the Uranian system, *Science*, *233*, 39, 1986.

Strobel, D. F., The photochemistry of hydrocarbons in the Jovian atmosphere, *J. Atmos. Sci.*, *30*, 489, 1973.

Strobel, D. F., and G. R. Smith, On the temperature of the Jovian thermosphere, *J. Atmos. Sci.*, *30*, 718, 1973.

Teifel, V. G., Methane abundance in the atmosphere of Uranus, *Icarus*, *53*, 389, 1983.

Tokunaga, A. T., G. S. Orton, and J. Caldwell, New observational constraints on the temperature inversions of Uranus and Neptune, *Icarus*, *53*, 141, 1983.

Tyler, G. L., D. N. Sweetnam, J. D. Anderson, J. K. Campbell, V. R. Eshleman, D. P. Hinson, G. S. Levy, G. F. Lindal, E. A. Marouf, and R. A. Simpson, Voyager 2 radio science observations of the Uranian system: Atmosphere, rings, satellites, *Science*, *233*, 79, 1986.

Wallace, L., and D. M. Hunten, The Lyman-alpha albedo of Jupiter, *Astrophys. J.*, *182*, 1013, 1973.

Warwick, J. W., et al., Voyager 2 Radio Observations of Uranus, *Science*, *233*, 102, 1986.

Yelle, R. V., L. R. Doose, M. G. Tomasko, and D. F. Strobel, Analysis of Raman scattered Ly-α emissions from the atmosphere of Uranus, *Geophys. Res. Lett.*, *14*(5), 483, 1987.

Yelle, R. V., J. C. McConnell, B. R. Sandel, and A. L. Broadfoot, The dependence of electroglow on the solar flux, *J. Geophys. Res.*, this issue.

Yung, Y. L., M. Allen, and J. P. Pinto, Photochemistry of the atmosphere of Titan: Comparison between model and observations, *Astrophys. J. Suppl. Ser.*, *55*, 465, 1984.

S. K. Atreya, Department of Atmospheric and Oceanic Science, Space Research Building, University of Michigan, Ann Arbor, MI 48109.

A. L. Broadfoot, F. Herbert, J. B. Holberg, B. R. Sandel, D. E. Shemansky, and R. V. Yelle, Lunar and Planetary West, University of Arizona, 901 Gould-Simpson Building, Tucson, AZ 85721.

P. N. Romani, NASA Goddard Space Flight Center, Mail Code 693.2, Greenbelt, MD 20771.

(Received March 30, 1987;
revised October 9, 1987;
accepted October 10, 1987.)